

# Tectonics

## RESEARCH ARTICLE

10.1029/2020TC006267

### Key Points:

- In the Lower Seve Nappe 1 km-thick mylonitic foliation formed at amphibolite facies conditions between ~460 and ~417 Ma
- Toward the base of the nappe the foliation is overprinted by a brittle-to-ductile fabric of greenschist facies conditions (~417 to 400 Ma)
- These fabrics formed due to protracted and long-lasting shearing during the exhumation and assembly of the Seve Nappe Complex

### Supporting Information:

- Supporting Information S1
- Table S1
- Table S2

### Correspondence to:

F. Giuntoli,  
francesco.giuntoli@gmail.com

### Citation:

Giuntoli, F., Menegon, L., Warren, C. J., Darling, J., & Anderson, M. W. (2020). Protracted shearing at midcrustal conditions during large-scale thrusting in the Scandinavian Caledonides. *Tectonics*, 39, e2020TC006267. <https://doi.org/10.1029/2020TC006267>

Received 23 APR 2020





Accepted 5 AUG 2020

Accepted article online 7 AUG 2020

©2020. American Geophysical Union.  
All Rights Reserved.

This is an open access article under the terms of the Creative Commons Attribution License, which permits use, distribution and reproduction in any medium, provided the original work is properly cited.

## Protracted Shearing at Midcrustal Conditions During Large-Scale Thrusting in the Scandinavian Caledonides

Francesco Giuntoli<sup>1,2</sup> , Luca Menegon<sup>3,1</sup> , Clare J. Warren<sup>4</sup> , James Darling<sup>5</sup> , and Mark W. Anderson<sup>1</sup>

<sup>1</sup>School of Geography, Earth and Environmental Sciences, Plymouth University, Plymouth, UK, <sup>2</sup>Department of Biological, Geological and Environmental Sciences, Università degli Studi di Bologna, Bologna, Italy, <sup>3</sup>The Njord Centre, Department of Geoscience, University of Oslo, Blindern, Norway, <sup>4</sup>Department of Environment, Earth and Ecosystems, Centre for Earth, Planetary, Space and Astronomical Research (CEPSAR), Open University, Milton Keynes, UK, <sup>5</sup>School of the Environment, Geography and Geosciences, University of Portsmouth, Portsmouth, UK

**Abstract** During continental collision, large tracts of crust are mobilized along major shear zones. The metamorphic conditions at which these zones operate, the duration of thrusting, and the deformation processes that facilitated hundreds of km of tectonic transport are still unclear. In the Scandinavian Caledonides, the Lower Seve Nappe displays a main mylonitic foliation with thickness of ~1 km. This foliation is overprinted by a brittle-to-ductile deformation pattern localized in C- and C'-type shear bands proximal to the tectonic contact with the underlying Särvi Nappe. Thermobarometry of amphibolites and micaschists suggests a first high-pressure stage at 400–500°C and 1–1.3 GPa recorded in mineral relics. The main mylonitic foliation developed under epidote amphibolite facies conditions along the retrograde path from 600°C and 1 GPa to 500°C and 0.5 GPa. Age dating of synkinematic titanite grains in the amphibolites indicates that this mylonitic fabric formed at around  $417 \pm 9$  Ma but older ages spanning 460–430 Ma could represent earlier stages of mylonitization. The shear bands developed at lower metamorphic conditions of 300–400°C and ~0.3 GPa. In the micaschists, the recrystallized grain size of quartz decreases toward the shear bands. Monomineralic quartz layers are eventually dismembered to form polyphase aggregates deforming by dominant grain size sensitive creep accompanied by slip in muscovite and chlorite. Plagioclase zoning truncations suggest that the shear bands originated by fracturing followed by ductile deformation. The results suggest protracted and long-lasting shearing under amphibolite to greenschist facies conditions during the juxtaposition, stacking, and exhumation of the Lower Seve Nappe.

### 1. Introduction

Thrusts in mountain belts localize much of the tectonic transport associated with crustal shortening during mountain building. They may be responsible for the juxtaposition of units characterized by remarkably contrasting tectonometamorphic histories (Bender et al., 2018; Gee, 1975; Giuntoli & Engi, 2016; Jolivet et al., 1998; Searle et al., 2008; Zwart, 1975). As they frequently form via several stages of deformation, shear zones often preserve multiple generations of overprinting mineral fabrics and relics, reflecting the evolution from higher to lower metamorphic grades (e.g., Papapavlou et al., 2018). Moreover, some fabrics display evidence of early stages of brittle deformation that has been later overprinted by crystal plastic deformation (e.g., Austrheim, 1987; Füsseis et al., 2006; Giuntoli, Menegon, & Warren, 2018; Mancktelow & Pennacchioni, 2005). In many cases cycles of brittle and ductile deformation appear to alternate due to the effect of different parameters, such as strain rate and stress variations, pore fluid pressure, mineral reactions, and associated weakening or hardening of the rock (Brander et al., 2012; Bukovská et al., 2016; Gerald & Stünitz, 1993; Giuntoli et al., 2020; Kjølseth et al., 2015; Menegon et al., 2013; Putnis & Putnis, 2007; Stünitz & Gerald, 1993). A robust constrain on the metamorphic conditions, deformation mechanisms, and timescale of shear zones activity is needed to better understand their role during orogenesis.

The Scandinavian Caledonides provide some of the best localities for investigating the relative roles and effects of these different inputs and controls on shearing, as they consist of a large-scale nappe stack of several tectonometamorphic units separated by thrusts that accommodated several hundreds of km of SE directed tectonic transport during continental collision (e.g., Gee et al., 2013; Roberts, 2003). Peak metamorphic

conditions and related ages are well documented in several of the tectonometamorphic units (e.g., Brueckner & Van Roermund, 2007; Janák et al., 2013; Ladenberger et al., 2013; Majka et al., 2014; Root & Corfu, 2012). However, fewer studies address the lower metamorphic grade evolution of such units, associated with their exhumation, juxtaposition, and the ESE directed tectonic transport over the Baltoscandian margin (e.g., Andersen, 1998; M. W. Anderson et al., 1992; Bender et al., 2018, 2019; Fossen & Rykkelid, 1992; Gilotti, 1989). Several open questions remain related to the pressure and temperature conditions of the low-grade metamorphism along the thrusts, the associated duration of thrusting, and the deformation processes that facilitated hundreds of km of tectonic transport.

In this study, we describe the evolution of metamorphic fabrics in a 1 km-long crustal section provided by the “Collisional Orogeny in the Scandinavian Caledonides (COSC-1; IGSN ICDP5054EHW1001)” drill core (Lorenz et al., 2015; see section 2). We reconstruct the first pressure-temperature-time-deformation (P-T-t-d) path for the Lower Seve Nappe. We constrain the metamorphic conditions, deformation mechanisms, and mineralogical changes related to these ductile and brittle fabrics using petrographic and microstructural analyses, thermodynamic modeling, electron backscattered diffraction analyses, and U-Pb geochronology on syn-kinematic titanite. Our results suggest that the nappe experienced protracted and long-lasting shearing from epidote amphibolite facies conditions to greenschist facies conditions, with strain localization toward the tectonic contact with the underlying Särvi Nappe. Our study provides detailed insight into the role of a major thrust in the exhumation and stacking of orogenic tectonometamorphic units.

## 2. Geological Setting

The Scandinavian Caledonides developed due to the Ordovician closure of the Iapetus Ocean and the subsequent Silurian to early Devonian subduction and continent collision of the Baltican plate below the Laurentian plate (e.g., Gee et al., 2008; Roberts, 2003; Roberts & Gee, 1985; Stephens, 1988). In the Scandinavian Caledonides, tectonic units were transported up to 400 km to the east during the collision, eventually creating a nappe stack of several allochthonous units on top of Autochthons Baltic Shield (Figures 1a and 1b; Gayer et al., 1987; Gee, 1975; Gee et al., 2010; Rice & Anderson, 2016). After emplacement, the nappe stack was folded into north trending synforms and antiforms, possibly related to either crustal extension and normal faulting or basement shortening occurring during the latest orogenic phases (Bergman & Sjöström, 1997; Rice & Anderson, 2016).

The Middle Allochthon, the target of this study, includes several basement units and associated metasediments representing the outermost Baltica margin and possibly includes units derived from an ocean-continent transition zone (e.g., Andréasson, 1994; Gee et al., 2008; Janák et al., 2006; Roberts, 2003; Stephens, 1988). The upper tectonic unit of the Middle Allochthon, the Seve Nappe Complex (SNC; e.g., Sjöström, 1983), crops out over a N-S distance of ~1,000 km and an W-E distance of ~200 km in the central part of the orogen (Figure 1; Andréasson, 1994).

In the Jämtland region, the SNC can be further subdivided into Lower, Middle, and Upper Seve nappes by the presence of internal thrust sheets (Zachrisson & Sjöstrand, 1990). The Lower Seve Nappe is mainly composed of micaschists, quartzites, and metapsammities with gneisses, metabasics, and with minor peridotites and serpentinites (Figure 1c). The Middle Seve Nappe is composed of similar lithologies but is overprinted by pervasive migmatization. Several parts of the Lower and Middle Seve preserve evidence of high pressure (HP) to ultrahigh pressure (UHP) metamorphism (summary in Figure 4 of Klonowska et al., 2016, and Figure 6 and Table 2 of Bender et al., 2018) spanning from ~1.1 GPa and 600°C up to 4 GPa and 800°C, within the stability field of coesite and diamond (Brueckner & van Roermund, 2004; Gilio et al., 2015; Janák et al., 2013; Klonowska et al., 2016, 2017; Majka et al., 2014; Van Roermund, 1985, 1989). The HP-UHP metamorphism is the manifestation of the Ordovician subduction of the SNC (Brueckner & Van Roermund, 2007; Ladenberger et al., 2013; Root & Corfu, 2012). To date, no evidence of (U)HP metamorphism has been recorded in the Lower Seve Nappe in central Jämtland.

In the Middle Seve Nappe, granulite and amphibolite facies metamorphism produced partial melting at 442–436 Ma (Ladenberger et al., 2013) and appear to postdate the HP-UHP stage, constrained around  $472 \pm 3$  Ma (Petrik et al., 2019). In the Lower Seve Nappe, a pervasive amphibolite facies foliation overprints the (U)HP fabric, where present, and represents the main metamorphic fabric. The (U)HP fabrics are composed of garnet, omphacite, phengite, rutile, and coesite (retrogressed in quartz) in the eclogites and quartz, phengite,

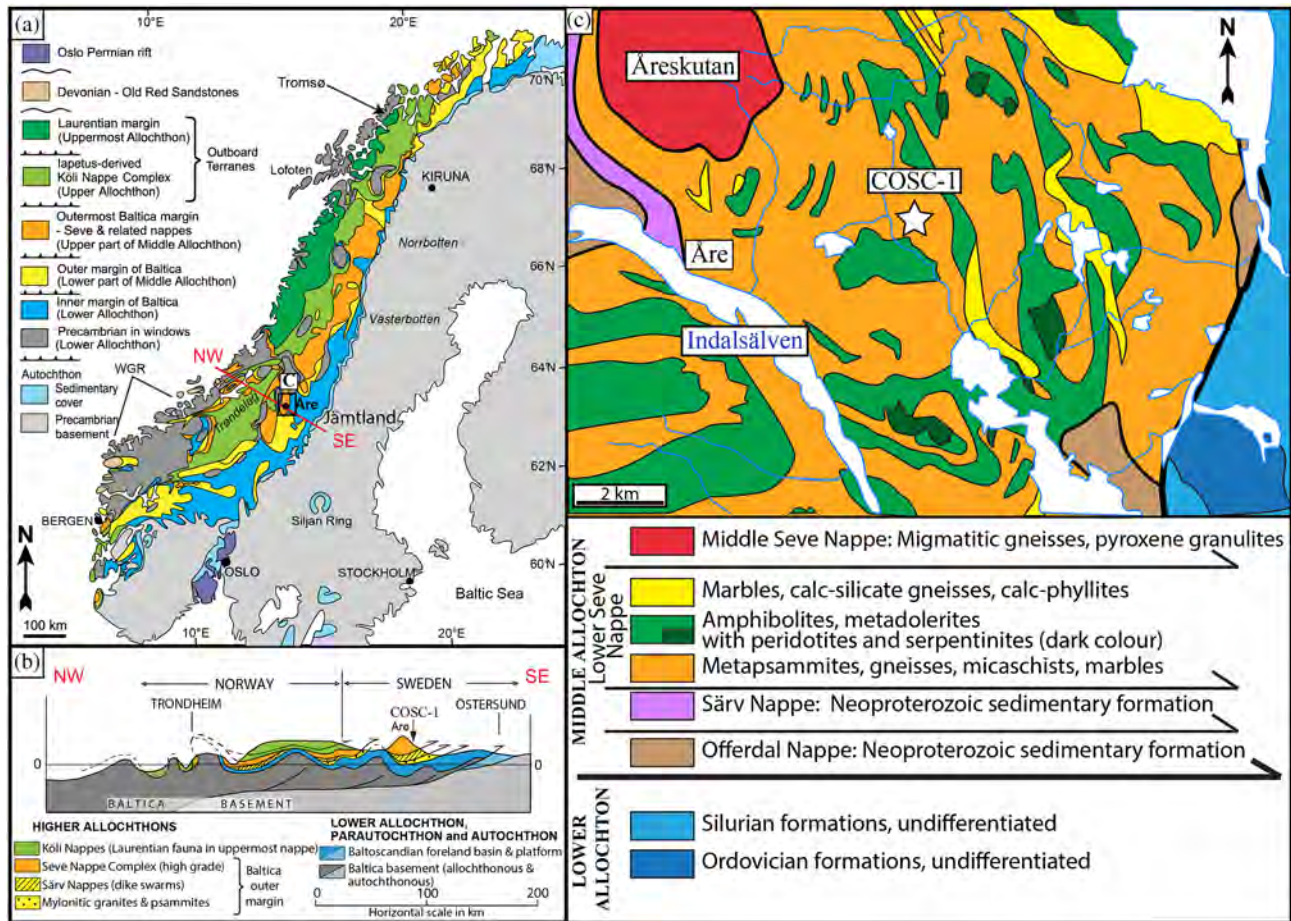


**Figure 1.** Geological setting of the Scandinavian Caledonides. (a) Tectonic map with inferred paleogeography of the nappes (modified after Gee et al., 2010). WGR = Western Gneiss Region. (b) Cross section marked in (a) with vertical exaggeration of 5X and approximate location of the COSC-1 borehole (modified after Gee et al., 2010). (c) Detail of the study area with location of the COSC-1 drilling site (modified after Strömberg et al., 1984).

garnet, jadeite, and rutile in the gneiss (Klonowska et al., 2016, and Fassmer et al., 2017, respectively). In the Åreskutan area, a recent field study identified two foliations: a main foliation of epidote amphibolite to upper-greenschist facies conditions partially overprinted by a lower grade foliation subparallel to it; both have dip direction toward E-NE and mean dip value of 30° (Bender et al., 2018). Both foliations develop stretching lineations that plunge shallowly and have mean azimuths of 88° and 103° for the higher and lower grade, respectively, and associated sense of shear top to the ESE (Bender et al., 2018). The epidote amphibolite facies metamorphic stage was constrained at ~600°C and 0.8–1 GPa in amphibolite (Giuntoli, Menegon, & Warren, 2018) and at 550°C and 0.2–0.5 GPa in micaschist (Arnbom, 1980) around ~430 Ma (Bender et al., 2019).

The COSC-1 borehole is located in the central Jämtland region, near Åre in Sweden (Lorenz et al., 2015; see location in Figures 1b and 1c). The drill core provides an almost complete section (recovery rate higher than 99%) through the Lower Seve Nappe. In detail, the core comprises alternating layers of felsic gneiss, calc-silicate, and amphibolite displaying narrow (mm-cm) and localized shear zones from the surface down to 1,700 m. Micaschist is more common below 1,700 m. The rocks show strongly deformed mylonitic fabrics from 1,700 m to the end of the core at 2,500 m depth (Giuntoli, Menegon, & Warren, 2018; Hedin et al., 2016). Below 2,350 m the core is composed of strongly deformed metasediments, interpreted as representing the basal shear zone juxtaposing the Lower Seve Nappe with the Särvi Nappe (Hedin et al., 2016; Lorenz et al., 2015). Acoustic televiewer data suggest that the regional foliation in the core is generally subhorizontal, with localized exceptions related to recumbent folds and boudinage (Wenning et al., 2017). The vergence of the lower-grade folds indicates that folding was in part coeval with top-to-the-ESE shearing at greenschist

facies conditions, as highlighted by field-based studies (Bender et al., 2018). Both in the field and in the core, lineations are oriented from E-W to SE-NW, with a mean trend/plunge  $100^{\circ}/20^{\circ}$ , in agreement with the Caledonian transport direction (Merz et al., 2019).

### 3. Materials and Methods

#### 3.1. Sample Preparation and Scanning Electron Microscopy

The drill core samples were oriented only with respect to the top of the borehole. The core declination reorientation allows to reorient the core with respect to the geographic north. This correction requires the identification of distinctive structures (e.g., folds), in both core scans and image logs (see Merz et al., 2019, for further details). This correction was not applied to the studied samples, as those were selected for their mylonitic fabrics that did not display distinctive structures essential for reorientation. Therefore, as core rotation around the vertical axis might have occurred during extraction, any reference to “dextral” sense of shear in the following sections is solely descriptive and does not carry information of actual direction of tectonic transport (see section 5.3 for discussion).

All scanning electron microscopy (SEM) analyses were performed on carbon-coated polished thin sections cut perpendicular to the foliation and parallel to the sample stretching lineation. Cathodoluminescence (CL) analyses were performed at the Open University (UK), using a FEI Quanta 200 three-dimensional SEM equipped with a Centaurus Deben panchromatic CL detector with a photo multiplier tube (Hamamatsu R316) characterized by sensitivity in the range of 400–1,200 nm. Analyses were conducted under high vacuum, using an accelerating voltage of 10 kV, a beam current of 3.3 nA, a working distance of 13 mm, and an electron source provided by a tungsten filament.

Backscattered electron (BSE) and electron backscattered diffraction (EBSD) analyses were conducted with a Jeol-7001FEG SEM at the Electron Microscopy Centre, Plymouth University (UK). EBSD patterns were acquired with a  $70^{\circ}$  tilted sample geometry, 20 kV accelerating voltage, a beam current of  $\sim 12.5$  nA, 18–23 mm working distance, and 1.3–1.7  $\mu\text{m}$  step size. Diffraction patterns were automatically indexed using AZtec (Oxford Instruments). Raw maps were processed with HKL Channel 5 software (Oxford Instruments), following the procedure illustrated in Prior et al. (1999, 2002, 2009). Crystallographic directions were plotted on pole figures (lower hemisphere of the stereographic projection), with X parallel to the stretching lineation and Z parallel to the pole of the mylonitic foliation, if not otherwise specified. Misorientation angle distributions were calculated for correlated pairs (with a shared boundary) and uncorrelated pairs and were compared with the theoretical random distribution. Misorientation axes were plotted in crystal coordinates (lower hemisphere of the stereographic projection) for misorientations of  $2$ – $10^{\circ}$  measured across boundaries between neighboring pairs (e.g., Prior et al., 2002; Wheeler et al., 2001). This misorientation range was chosen to investigate the nature of low-angle boundaries (e.g., Neumann, 2000). EBSD maps include phase maps, grain size maps (where the grain size is defined as the diameter of the equivalent circle), and grain orientation spread (GOS) maps. GOS is a measure of the internal strain of a grain defined as the average misorientation angle between each pixel in a grain and that grain's mean orientation (Wright et al., 2011).

#### 3.2. Electron Probe Microanalyzer

EPMA analyses were conducted at the Open University (UK), using a five-spectrometer Cameca SX100. Wavelength dispersive spectrometers (WDS) provided data for both spot analyses and X-ray maps. Spot analyses were first acquired for each mineral phase, before X-ray maps were acquired from the same area. Spot analyses were performed with 20 KeV accelerating voltage, 20 nA specimen current, and 2  $\mu\text{m}$  beam diameter. Ten oxide compositions were measured, using natural standards: K-feldspar ( $\text{SiO}_2$ ,  $\text{Al}_2\text{O}_3$ , and  $\text{K}_2\text{O}$ ), bustamite ( $\text{CaO}$  and  $\text{MnO}$ ), hematite ( $\text{FeO}$ ), forsterite ( $\text{MgO}$ ), jadeite ( $\text{Na}_2\text{O}$ ), rutile ( $\text{TiO}_2$ ), and apatite ( $\text{P}_2\text{O}_5$ ). A ZAF matrix correction routine was applied; uncertainty on major element concentrations was  $<1\%$ . X-ray maps were acquired with 15 KeV accelerating voltage, 100 nA specimen current, dwell times of 70–100 ms, and step size of 5  $\mu\text{m}$ . Ten elements (Si, Ti, Al, Fe, Mn, Mg, Na, Ca, K, and P) were measured at the specific wavelength in two series. Intensity X-ray maps were standardized to concentration maps of oxide weight percentage using spot analyses as internal standard. X-ray maps were processed using XMapTools 2.6.4 (Lanari et al., 2014). Quantitative X-ray maps were used as input for isochemical phase diagram computation, following the strategy of Lanari & Engi (2017; see the following section).

### 3.3. Geothermobarometry

#### 3.3.1. Isochemical Phase Diagrams (Pseudosections)

Isochemical equilibrium phase diagrams were computed using the Gibbs free energy minimization algorithm Theriak-Domino (De Capitani & Brown, 1987; de Capitani & Petrakakis, 2010). The thermodynamic database of Berman (1988) with subsequent updates collected in JUN92.bs was used, together with the following solution models: Berman (1990) for garnet, Nagel et al. (2002) for staurolite, Fuhrman and Lindsley (1988) for feldspar, Keller et al. (2005) for white mica, and ideal mixing models for amphibole (Mäder et al., 1994; Mäder & Berman, 1992) and chlorite (Hunziker, 2003).  $\text{Fe}^{3+}$  was ignored because of the lack of analytical data and suitable ferric endmembers in solid solution models. Local bulk compositions were obtained using standardized X-ray maps (section 3.2) following the procedure described in Lanari and Engi (2017). As indicated by those authors, the chosen areas should be representative of the equilibrium volumes that were examined. Thus, it is important to evaluate if the results of thermodynamic modeling match the observed parageneses in term of modal amount of the mineral phases and their chemical compositions. The amounts of  $\text{H}_2\text{O}$  component used in the computations were estimated from the  $\text{H}_2\text{O}$  contents needed to stabilize the amount of hydrous minerals extracted from the local bulk composition. These values were in line with the measured loss of ignition values (1.4–4 wt%) of the present-day samples. Each garnet growth zone was sampled from the standardized X-ray maps. Successively, the program GrtMod (Lanari et al., 2017) was used to find the best analytical solution between measured and modeled composition of garnet. This computer program used an iterative approach that refined the P-T conditions for successive garnet growth zones. The program interacts with Theriak and uses the same thermodynamic database as the isochemical equilibrium phase diagrams (for further details, see Giuntoli, Lanari, et al., 2018).

#### 3.3.2. Amphibole-Plagioclase Thermobarometry

Temperature was estimated using Holland and Blundy (1994) geothermometer, which uses the equilibrium element exchange between amphibole and plagioclase pairs, constrained for silica-saturated and silica-rich igneous and metamorphic rocks in the range of 0.1–1.5 GPa and 400–1,000°C. Pressure was estimated using Bhadra and Bhattacharya (2007) and Anderson and Smith (1995) geobarometers. The first geobarometer is based on element distribution between amphibole and plagioclase pairs in equilibrium. Experimental data were acquired on silica-saturated assemblages in the P-T range of 0.1–1.5 GPa and 650–950°C. The second geobarometer is based on the increase of Al in hornblende with increasing pressure and is calibrated on experimental data at 675°C and 760°C.

#### 3.3.3. Chlorite and White Mica Multiequilibrium

To constrain the P-T conditions of retrograde stages, multiequilibrium computations of the high-variance assemblages involving chlorite and white mica were performed, using the standard state properties and solid solution models of Vidal et al. (2005, 2006) for chlorite, Dubacq et al. (2010) for phengite, and the program ChlMicaEqui (Lanari, 2012; Lanari et al., 2012). The activity of  $\text{H}_2\text{O}$  was set to unity. In detail, the thermobarometry was based on the chlorite + white mica + quartz +  $\text{H}_2\text{O}$  equilibrium. The P and T of formation for each chlorite and white mica couple, as well as their respective  $X_{\text{Fe}^{3+}}$  values, were estimated by minimizing the square root of the sum of  $(\Delta G_{\text{reaction}})^2$  for the following six equilibria:

1.  $-4$  Clinocllore +  $4$  Daphnite  $- 5$  Fe-Amesite +  $5$  Mg-Amesite.
2.  $14$  alpha-Quartz  $- 4$  Daphnite +  $5$  Fe-Amesite +  $3$  Mg-Amesite  $- 6$  Sudoite +  $8$  WATER.
3.  $-10$  Mg-Celadonite +  $15$  alpha-Quartz  $- 2$  Daphnite +  $10$  Fe-Celadonite +  $2$  Mg-Amesite  $- 4$  Pyrophyllite + Sudoite.
4.  $75$  alpha-Quartz  $- 2$  Clinocllore +  $2$  Daphnite  $- 10$  Fe-Celadonite +  $10$  Muscovite  $- 20$  Pyrophyllite +  $5$  Sudoite.
5.  $-5$  Mg-Celadonite + Clinocllore +  $4$  Daphnite  $- 5$  Fe-Amesite +  $5$  Muscovite.
6.  $2$  Fe-Amesite  $- 8$  Fe-Celadonite +  $13$  Mg-Amesite +  $8$  Muscovite +  $14$  Pyrophyllite  $- 26$  Sudoite +  $30$  WATER.

### 3.4. U-Pb Geochronology by Laser Ablation-Inductively Coupled Plasma-Mass Spectrometry

Titanite grains were analyzed for U-Pb isotopes using an ASI RESOLUTION 193 nm ArF excimer laser coupled to a quadrupole Agilent 7500cs inductively coupled plasma-mass spectrometry (ICP-MS) at the University of Portsmouth, following the procedure described in Papapavlou et al. (2017). The spot size was  $30 \mu\text{m}$ , the laser fluence was approximately  $3 \text{ J/cm}^2$  and the frequency 2 or 3 Hz. A sample-standard bracketing method was

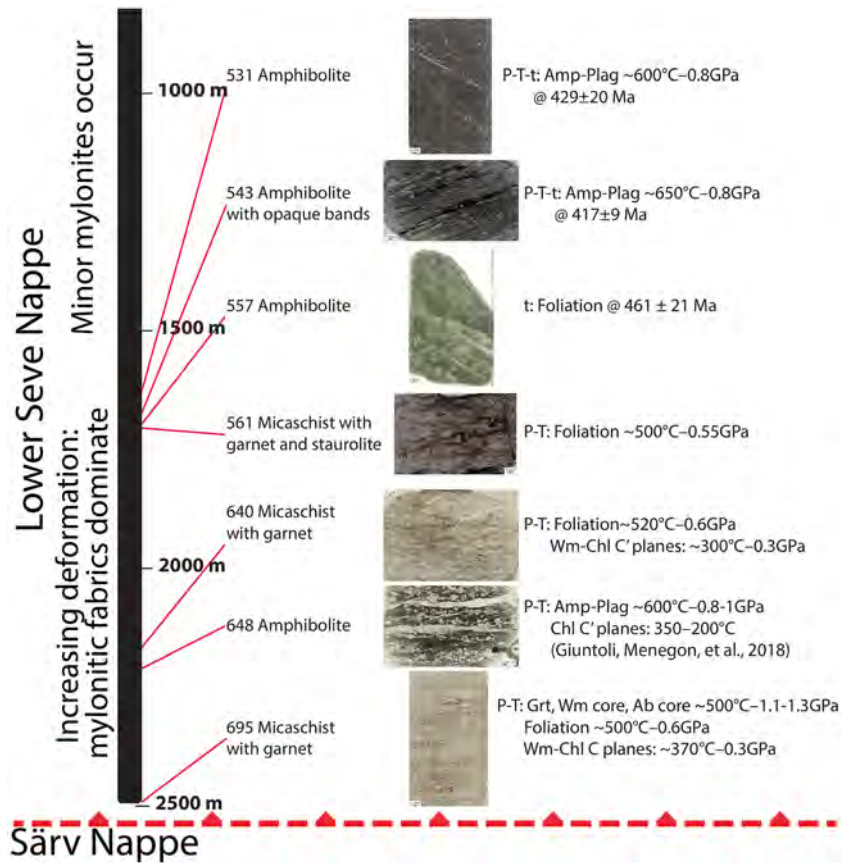


**Figure 2.** Location of the studied samples along the drill core and summary of the P-T-t data for the Lower Seve Nappe (this study; see text for details and discussion). The inferred contact with the underlying Särv Nappe is marked by the dashed line. Depth values are referred to meters from the surface.

used to correct for mass fractionation, using Khan titanite as the primary standard (ID-TIMS age of  $522.2 \pm 2.2$  Ma; Heaman, 2009). Downhole U-Pb elemental fractionation was corrected using an exponential downhole correction fit to the time-resolved data for each analysis. A  $^{207}\text{Pb}$ -based correction scheme was applied to the variably common lead-bearing primary standard using the Vizuage\_UcomPbine add-in for Iolite (Chew et al., 2014). MKED-1 titanite was analyzed as a secondary standards to evaluate accuracy of the method, and the resulting weighted mean  $^{206}\text{Pb}/^{238}\text{U}$  age ( $1,523.1 \pm 4.0$  Ma) and concordia age ( $1,523.7 \pm 5.5$  Ma) are within uncertainty of reference values (ID-TIMS  $^{206}\text{Pb}/^{238}\text{U}$  age of  $1,521.02 \pm 0.55$  Ma; Spandler et al., 2016). The  $^{238}\text{U}/^{206}\text{Pb}$  and  $^{207}\text{Pb}/^{206}\text{Pb}$  isotopic ratios for each analysis are presented uncorrected for common lead in Tera-Wasserburg concordia diagram using IsoplotR (Vermeesch, 2018).

## 4. Results

### 4.1. Petrography and Microstructures

The micaschists and amphibolites from the lower part of the drill core (1,500–2,500 m; Figure 2) display a subhorizontal to moderately dipping main fabric (S).

#### 4.1.1. Micaschists

The three micaschist samples were collected at ~1,700 m (Sample 561), 2,170 m (Sample 640), and 2,500 m (Sample 695; Table S1; Figures 2 and 3) depths, allowing the variation of fabrics through different levels of the nappe to be observed. The main S foliation consists of muscovite, biotite, quartz, plagioclase, and epidote. Isolated porphyroclasts of plagioclase and biotite and muscovite mica fish grains are wrapped by the foliation (Figure 3). The foliation is mylonitic, and a stretching lineation is observable in the hand specimens and is marked by rods of plagioclase and quartz and by elongated trails of muscovite and biotite. Both

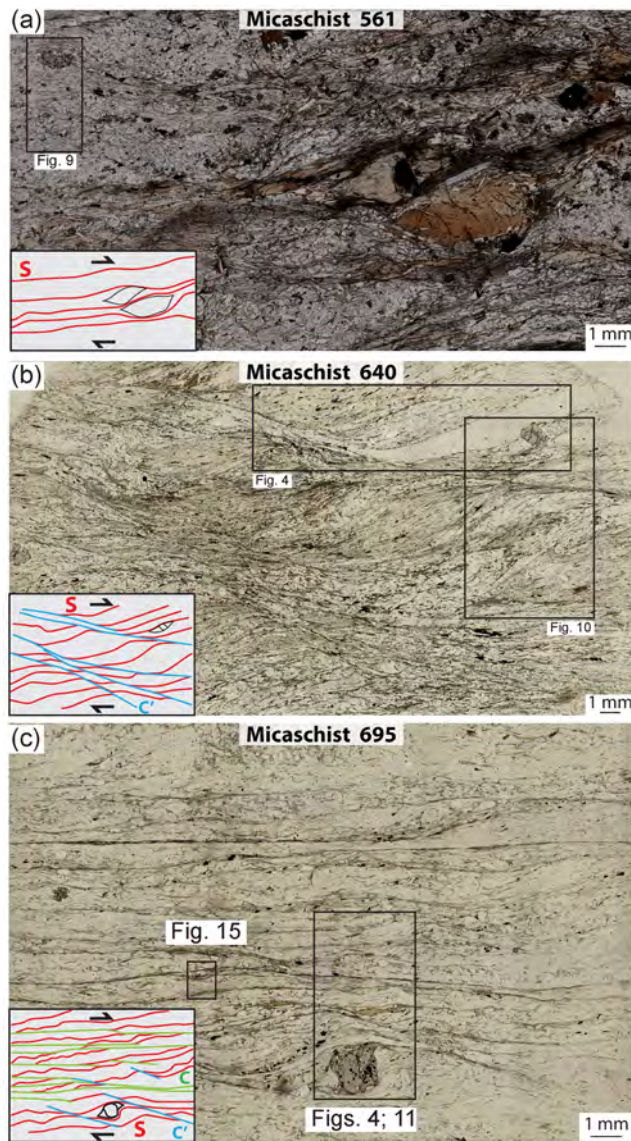


**Figure 3.** Thin section scans of micaschist samples (plane-polarized light). In the microstructural sketches and in the following figures, the red lines indicate the mylonitic S fabric of epidote amphibolite facies conditions, the green and light blue lines indicate the C- and C'-type shear bands, and the arrows the sense of shear. (a–c) Samples 561, 640, and 695, respectively. The black rectangles indicate the location of the following figures.

brown (Figures 6a and 7a). The core is darker than the rim in BSE images (Figure 6c). Plagioclase cores are brighter in CL than the rims and display polysynthetic twinning (Figures 6b and 7b). The rims form asymmetric tails around the core, compatible with a dextral sense of shear, kinematic consistent with the main foliation. Like in the micaschists, a main shear plane is not visible in thin section, as the deformation is more diffuse.

Opaque minerals include ilmenite, up to 1 mm in size, and minor magnetite and pyrite, the latter cored by chalcopyrite. In Sample 543 ilmenite and pyrite form layers parallel to the mylonitic foliation (Figure 5b). In all the samples, ilmenite grains are elongate and lie parallel to the mylonitic foliation. Ilmenite is rimmed by titanite, which also grows in the ilmenite boudin necks (Figures 7f and 8a). Titanite displays intergrowths with amphibole and plagioclase rims. A few titanite grains occur as elongate grains parallel to the main

generations of micas (i.e., the mica fish and the grains along the foliation) display undulose extinction and bending (Figure 4). Millimeter-sized garnet and staurolite are present in Sample 561. Dextral sense of shear is observed (Figure 3; note that the sense of shear is solely descriptive as explained in section 3.1). Accessory phases include pyrite, ilmenite, magnetite, apatite, calcite, and zircon. In Sample 695, plagioclase displays dark porphyroclastic core and bright rim in CL images (Figures 4g and 4h). The rims form asymmetric tails around the core, compatible with a dextral sense of shear, kinematic consistent with the main foliation. Microfractures are frequent in the cores and are sealed by plagioclase with a similar luminescence as the rim, as described in Giuntoli, Menegon, and Warren (2018) (Figures 4g and 4h). Chlorite crystallizes in the garnet asymmetric pressure shadows in Sample 695, defining a dextral sense of shear.

The mylonitic S foliation is deformed by discrete 1 mm-spaced C'-type shear bands defined by chlorite and white mica (Sample 640; Figures 3 and 4), which deform into sigmoidal-shaped white mica and biotite grains and quartz ribbons. These in turn define the main foliation. Toward the bottom of the drill core (e.g., Sample 695), C- and C'-type shear bands are more discrete and pervasive. Their spacing of some hundreds of  $\mu\text{m}$  produces a composite S-C-C' fabric (Figure 3c). Locally, these C and C' planes are extremely sharp and cut the surrounding minerals: for example, in plagioclase grains these planes truncate both growth zones (Figure 4g). The C- and C'-type shear bands display sense of shear identical to the main foliation. Note that even if the shear zone boundaries were not observed, the thickness of the mylonitic foliation ( $\sim 1$  km) and the high degree of transposition throughout the drill core suggest that the shear zone margins are likely parallel to the mylonitic foliation itself.

#### 4.1.2. Amphibolites

Three mafic amphibolite samples were collected at depths of  $\sim 1,625$  m (Sample 531), 1,660 m (543), and 1,700 m (557; Table S1; Figures 2 and 5) and were compared with the results from amphibolite Sample 648 collected at a depth of  $\sim 2,200$  m described in Giuntoli, Menegon, and Warren (2018).

In the amphibolites the mylonitic S foliation is defined by amphibole, plagioclase, chlorite, quartz, epidote, and ilmenite wrapping around bigger plagioclase porphyroclasts, with a dextral sense of shear (Samples 531 and 543; Figures 5–7). Like in the micaschists, a stretching lineation is present on the hand specimen and is marked by the mineral defining the foliation. Rare zircon and apatite are present. Quartz and calcite veins occur subparallel to the mylonitic foliation. Amphibole displays a less pleochroic core, which varies from light green to light brown absorption colors, and a more pleochroic rim, which varies from dark green to dark

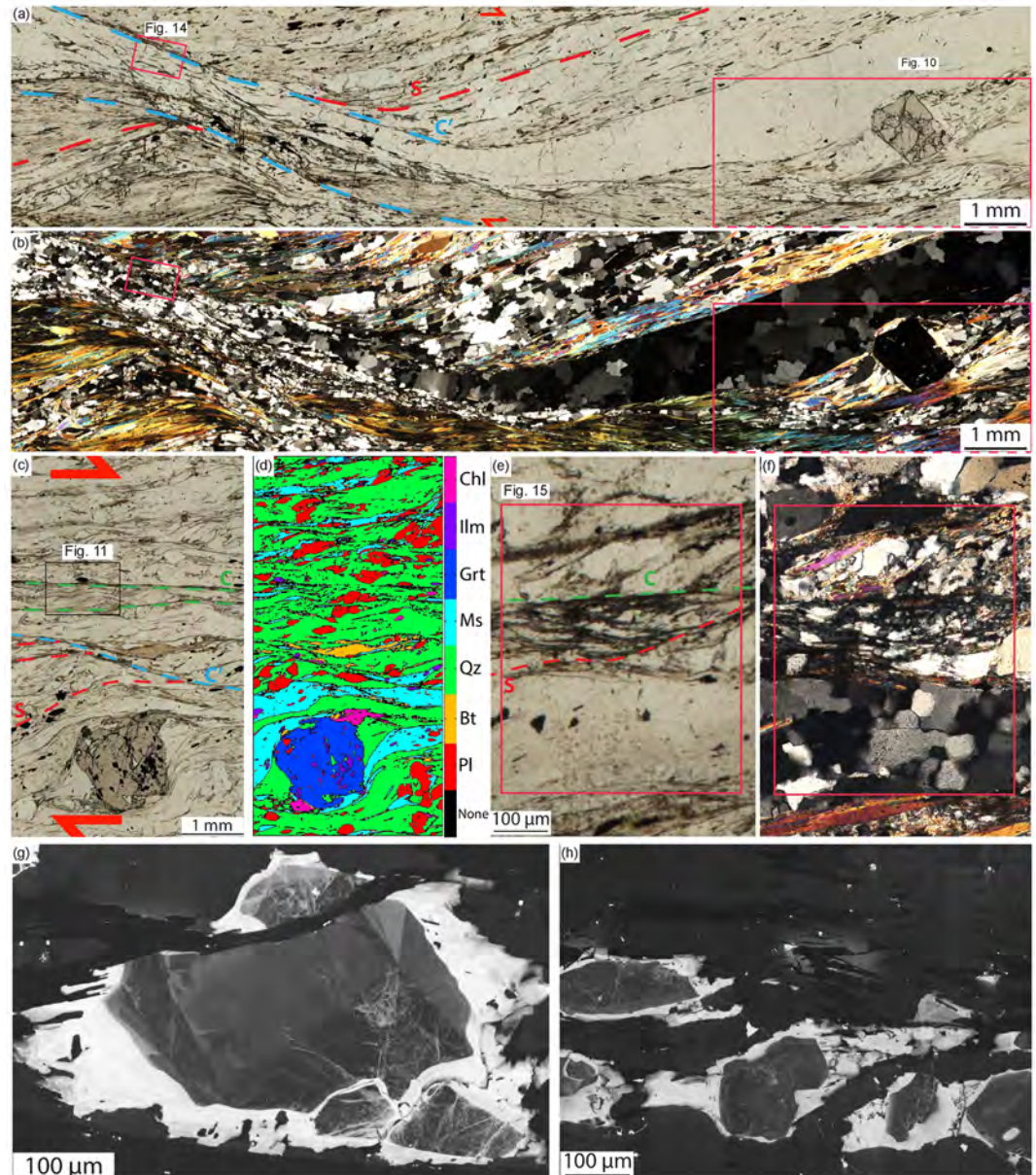


**Figure 4.** (a–f) Main mylonitic foliation of epidote amphibolite facies condition (red lines) overprinted by C- and C'-type shear bands of greenschist facies conditions (green and light blue lines, respectively) in garnet micaschists. (a, b) Quartz monomineralic layer displays a decrease in grain size in correspondence of the C' band, with a dextral sense of shear; plane and crossed-polarized light photo, respectively (micaschist Sample 640). (c) S structure overprinted by C and C' planes indicating a dextral sense of shear, plane-polarized light photo (micaschist Sample 695). The black rectangle indicates the location of the enlargement on C-type shear bands of Figure 11. (d) X-ray map showing the mineral phases. (e, f) Detail of the C planes with location of the EBSD map of Figure 15 (red square; plane and crossed-polarized light photo, respectively). (g, h) CL images highlighting plagioclase microstructures of micaschist Sample 695. The porphyroclastic core is dark and displays a network of fractures few  $\mu\text{m}$  thick and up to several hundreds of  $\mu\text{m}$  long, sealed by a plagioclase that has the same brightness as the syn-kinematic rim. The asymmetry of the rims is consistent with a dextral sense of shear. In (g) both core and rim are cut by the C shear band.

foliation, are up to some hundreds of  $\mu\text{m}$  in size, and do not have ilmenite cores (Figure 8b). BSE images of titanite grains display homogeneous brightness (Figures 7g, 7h, and 8f), with minor patchy areas (bottom part of Figure 8h). Standardized X-ray maps for titanite show some patchy variation  $<2$  weight percentage in the oxides of the mayor elements ( $\text{TiO}_2$ ,  $\text{CaO}$ , and  $\text{SiO}_2$  in Figures 6g–6i, respectively). These data do not highlight concentric zoning reflecting a core to rim growth.



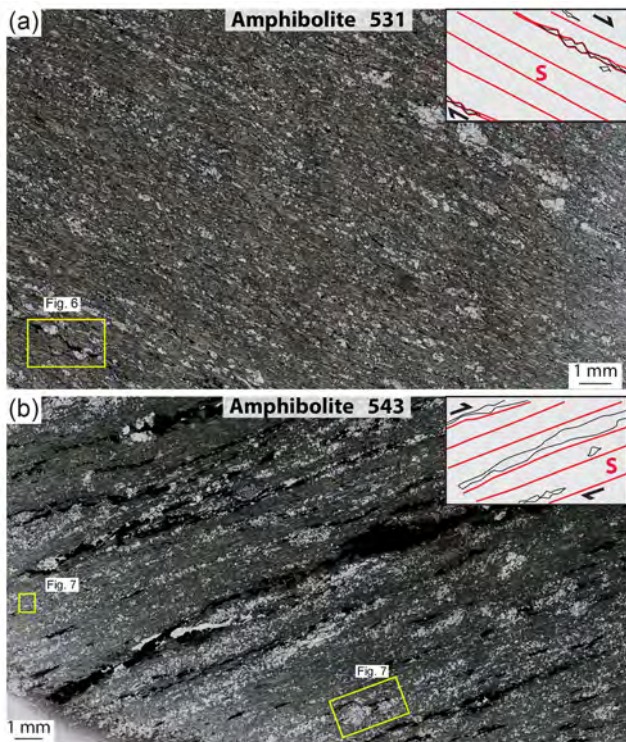


**Figure 5.** Thin section scans of amphibolite Samples 531 and 543, respectively (plane-polarized light). The mylonitic S foliation wraps around plagioclase porphyrocrysts highlighting a dextral sense of shear.

## 4.2. Geothermobarometry

### 4.2.1. Isochemical Phase Diagrams on Micaschists

Local bulk compositions used for isochemical phase diagrams computation are available in Table S2 in the supporting information. The chosen areas match with the standardized X-ray maps of Figures 9–11. In all the micaschist samples, standardized X-ray maps for garnet highlight concentric zoning, with a core richer in  $X_{Sps}$  than the rim (Figures 9–11; Table 2). Muscovite is characterized by some relic phengitic cores that are richer in Si than the rims, the latter describing the main foliation. Plagioclase shows cores that are poorer in  $X_{Ab}$  than the rims in Sample 561 (Figure 9f); this zoning is inverse in Sample 695 (Figures 11d and 11o; Table 3).

In Sample 561 GrtMod results predict the garnet core to be stable at  $\sim 0.4$  GPa and  $410^\circ\text{C}$  (Figure 12a; the error bars departing from filled ellipses show the P-T uncertainty related to the analytical error of the garnet composition; see Lanari et al., 2017). The modeled composition is  $Alm_{0.71}, Prp_{0.09}, Grs_{0.06}, Sps_{0.14}$ ; the measured composition is available in Table 2. The garnet rim is predicted stable at  $\sim 0.6$  GPa and  $430^\circ\text{C}$  (modeled composition:  $Alm_{0.71}, Prp_{0.12}, Grs_{0.09}, Sps_{0.09}$ ), but this result overlaps the garnet core within uncertainty. Thermodynamic modeling predicts a total of 8 vol% of garnet stable (estimated mineral assemblages in thin section available in Table S2). P-T conditions of garnet rim match with Si apfu isopleths of muscovite rim,  $X_{Ab}$  isopleths of plagioclase rims, and  $X_{Mg}$  isopleths of staurolite and biotite (the latter within error). In summary, based on the intersections of the previous data, the most likely conditions computed for the development of the foliation are  $\sim 0.55$  GPa and  $500^\circ\text{C}$  (red dashed ellipsis in Figure 12a representing the P-T conditions of the metamorphic stages

best fitting with the observed paragenesis and the computed isopleths). The predicted assemblage conforms to the minerals observed in thin section, except that kyanite was not detected in thin section (1.9 vol% predicted) and epidote is not predicted stable but is observed in thin section ( $\sim 2$  vol%; Table S2). Si apfu isopleths of phengitic muscovite cores would suggest a higher-pressure stage at  $\sim 1.1$  GPa (red dashed ellipsis in Figure 12a), similarly to the other samples (see the next paragraphs). Plagioclase core  $X_{Ab}$  isopleths could indicate a higher-temperature stage of  $\sim 650^\circ$ , although no other evidence is present for such higher-temperature stage in the studied micaschist samples (see discussion section 5.1).

In Sample 640 the garnet core and rim are modeled to be stable at similar pressure and temperature conditions of  $\sim 0.58$  GPa and  $520^\circ\text{C}$  and  $0.6$  GPa and  $530^\circ\text{C}$  (Figure 12b, modeled composition:  $Alm_{0.69}, Prp_{0.06}, Grs_{0.18}, Sps_{0.07}$  and  $Alm_{0.70}, Prp_{0.06}, Grs_{0.19}, Sps_{0.05}$ ). A total of  $\sim 2$  vol% of garnet is predicted to crystallize. These P-T conditions match, within error, the Si apfu isopleths of muscovite marking the foliation,  $X_{Ab}$  isopleths of plagioclase, and  $X_{Mg}$  isopleths of biotite (red dashed ellipsis in Figure 12b). The Si apfu isopleths of the rare phengitic muscovite cores suggest a higher-pressure stage. The predicted assemblage matches the minerals observed (Table S2).

In Sample 695 the garnet core and rim are found to be stable at the same P-T conditions of  $\sim 1.2$  GPa and  $510^\circ\text{C}$  (Figure 12c, modeled compositions:  $Alm_{0.63}, Prp_{0.04}, Grs_{0.18}, Sps_{0.15}$  and  $Alm_{0.65}, Prp_{0.04}, Grs_{0.18}, Sps_{0.13}$ ). A total of  $\sim 9$  vol% of garnet is predicted to crystallize. These conditions match with Si apfu isopleths of phengitic muscovite cores and with  $X_{Ab}$  isopleths of plagioclase core. Si apfu isopleths of muscovite marking the foliation intersect the  $X_{Mg}$  isopleths of biotite around  $0.6$  GPa and  $500^\circ\text{C}$ . At these metamorphic conditions the predicted assemblage is consistent with the minerals observed in thin section. For the three micaschist samples inferred P-T paths are indicated with the purple dashed line in Figure 12. These trajectories are drawn linking the red dashed ellipses and the chlorite and white mica multiequilibrium results (in Samples 640 and 695; see section 4.2.3).

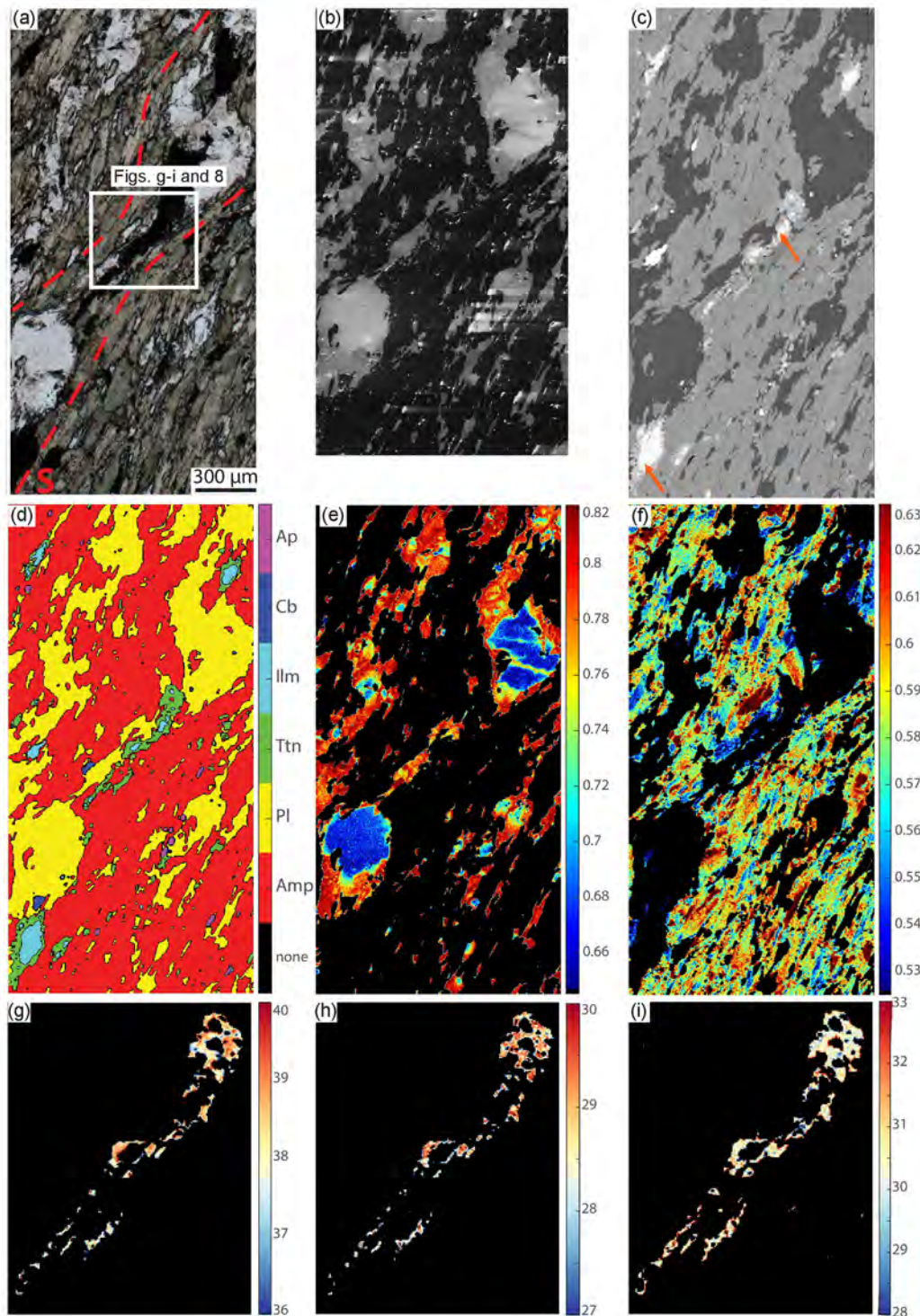


**Figure 6.** Microstructure and chemical data of amphibolite Sample 531. The photos and maps were rotated of 90° counterclockwise from the original orientation of the sample in the drill core for acquisition and graphic purposes (see original orientation in Figure 5a). (a) Optical photo showing the pressure shadow between two plagioclase porphyrocrysts. Amphibole has a less pleochroic core (light brown) and a more pleochroic rim (dark green), plane-polarized light. The white square indicates the location of the EBSD map (Figure 8). (b) CL image of bright plagioclase porphyroclastic core with darker fractures and syn-kinematic rims; compare with (e). (c) BSE image with bright ilmenite rimmed by titanite (arrows). (d–i) Standardized X-ray maps. (d) Map of the mineral phases. (e) Plagioclase  $X_{Ab}$  map displays low  $X_{Ab}$  porphyroclastic cores and high  $X_{Ab}$  syn-kinematic rims. Note that the fractures in the core are sealed by a plagioclase richer in albite content and similar to the rim composition. (f) Amphibole  $X_{Mg}$  map highlighting a richer  $X_{Mg}$  relic core and a poorer syn-kinematic rim. (g–i) Titanite oxide weight percentages of  $TiO_2$ ,  $CaO$ , and  $SiO_2$ , respectively.

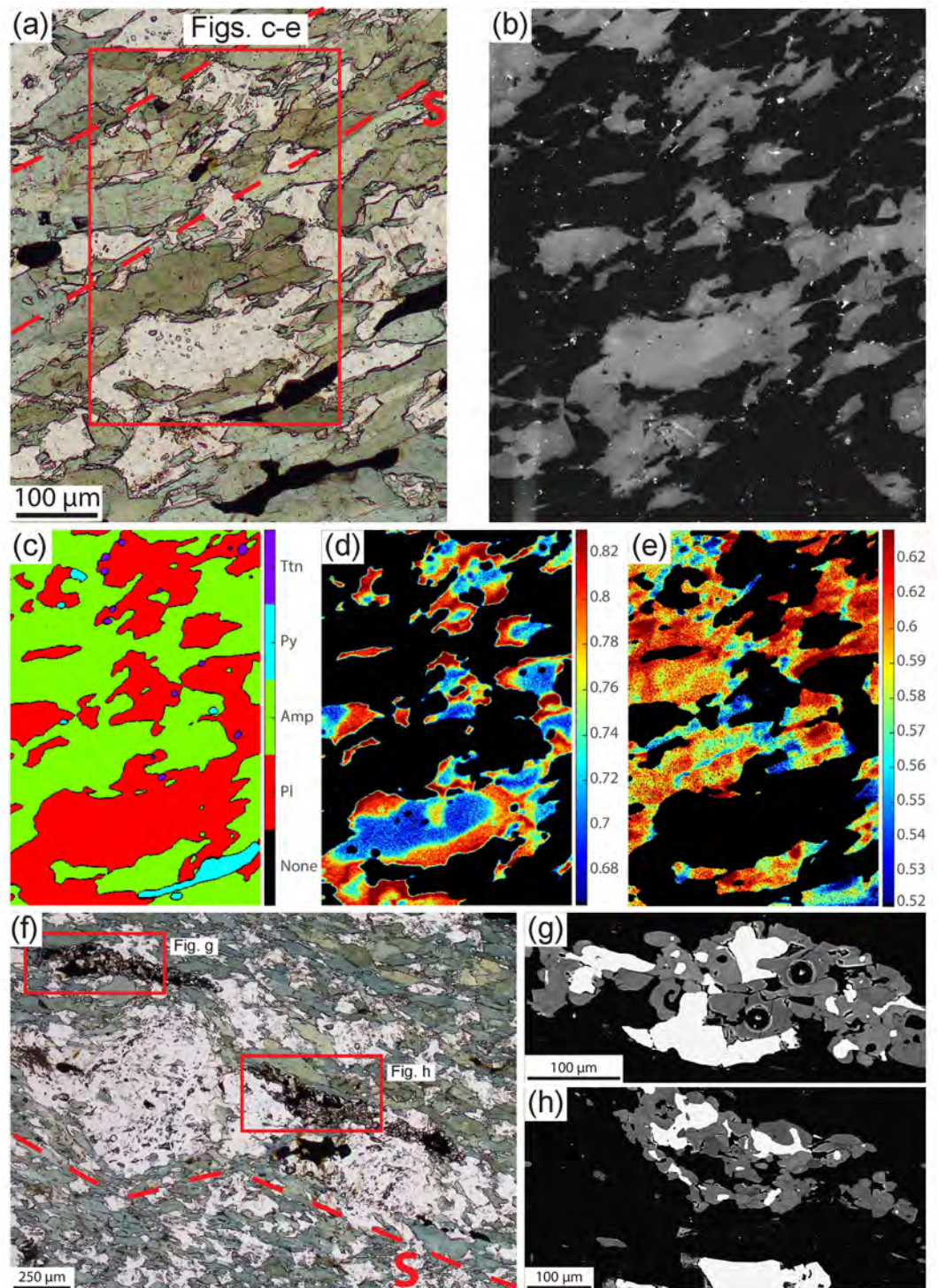


**Figure 7.** Microstructure and chemical data of amphibolite Sample 543. (a) Optical photo, plane-polarized light. The red rectangle indicates the location of X-ray maps c–e. (b) CL image of bright plagioclase relic cores and darker syn-kinematic rims; compare with (d). (c–e) Standardized X-ray maps. (c) Map of the mineral phases. (d) Plagioclase  $X_{Ab}$  map displays low  $X_{Ab}$  relic cores and high  $X_{Ab}$  syn-kinematic rims. (e) Amphibole  $X_{Mg}$  map highlighting a richer  $X_{Mg}$  relic core and a poorer syn-kinematic rim. (f) Titanite rimming ilmenite lengthened as the main foliation; optical photo, plane-polarized light. (g, h) BSE images highlighting bright ilmenite, with lobate edges, surrounded by darker titanite grains. Note the laser ablation pits.

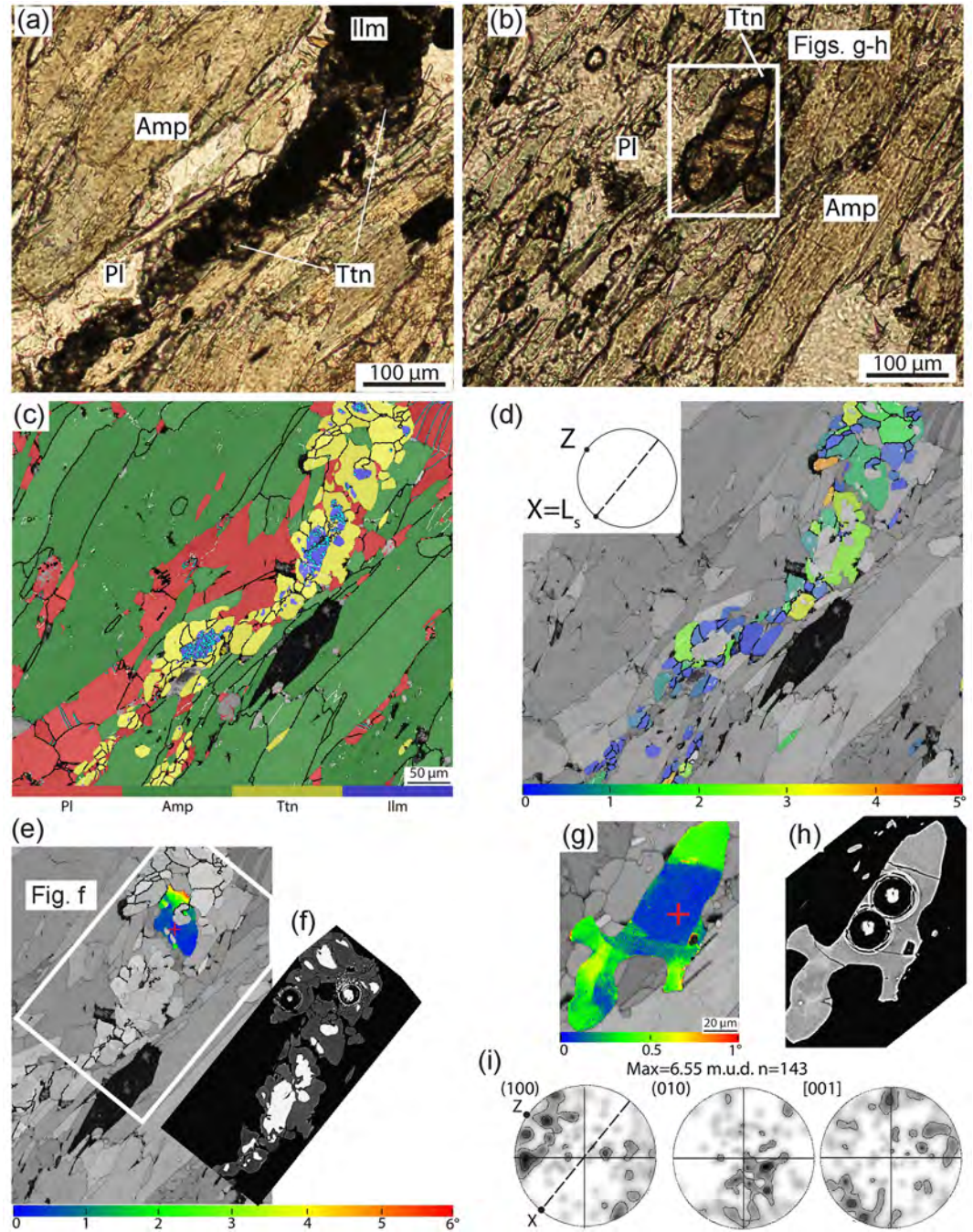


**Figure 8.** Microstructural characterization of titanite grains in amphibolite Sample 531. (a) Detail of Figure 6 displaying ilmenite boudinated with titanite growing in the boudin necks. (b) Titanite grains intergrown with amphibole and plagioclase lengthened as the mylonitic main foliation. Optical photos, plane-polarized light. (c) EBSD phase map. Note the ilmenite rimmed by titanite. White lines indicate low-angle boundaries ( $2\text{--}10^\circ$ ), black lines high-angle boundaries ( $>10^\circ$ ), and light blue lines twin boundaries in ilmenite ( $180^\circ$  rotation about an axis parallel to  $[100]$  axis). (d) Titanite GOS map, suggesting that it has very low internal strain. (e and g) Titanite texture component maps and BSE images (f and (h)). (i) Titanite pole figures of map (c). Contouring is 1.

#### 4.2.2. Amphibole-Plagioclase Thermobarometry on Amphibolites

In the amphibolite samples, the standardized X-ray maps for plagioclase highlight poorer  $X_{Ab}$  porphyroclastic cores (0.64–0.74) and richer  $X_{Ab}$  syn-kinematic rims (0.74–0.82, Figures 6e and 7d; Table 3), results that perfectly match with the CL images (Figures 6b and 7b). Some fractures are visible in the core and are sealed

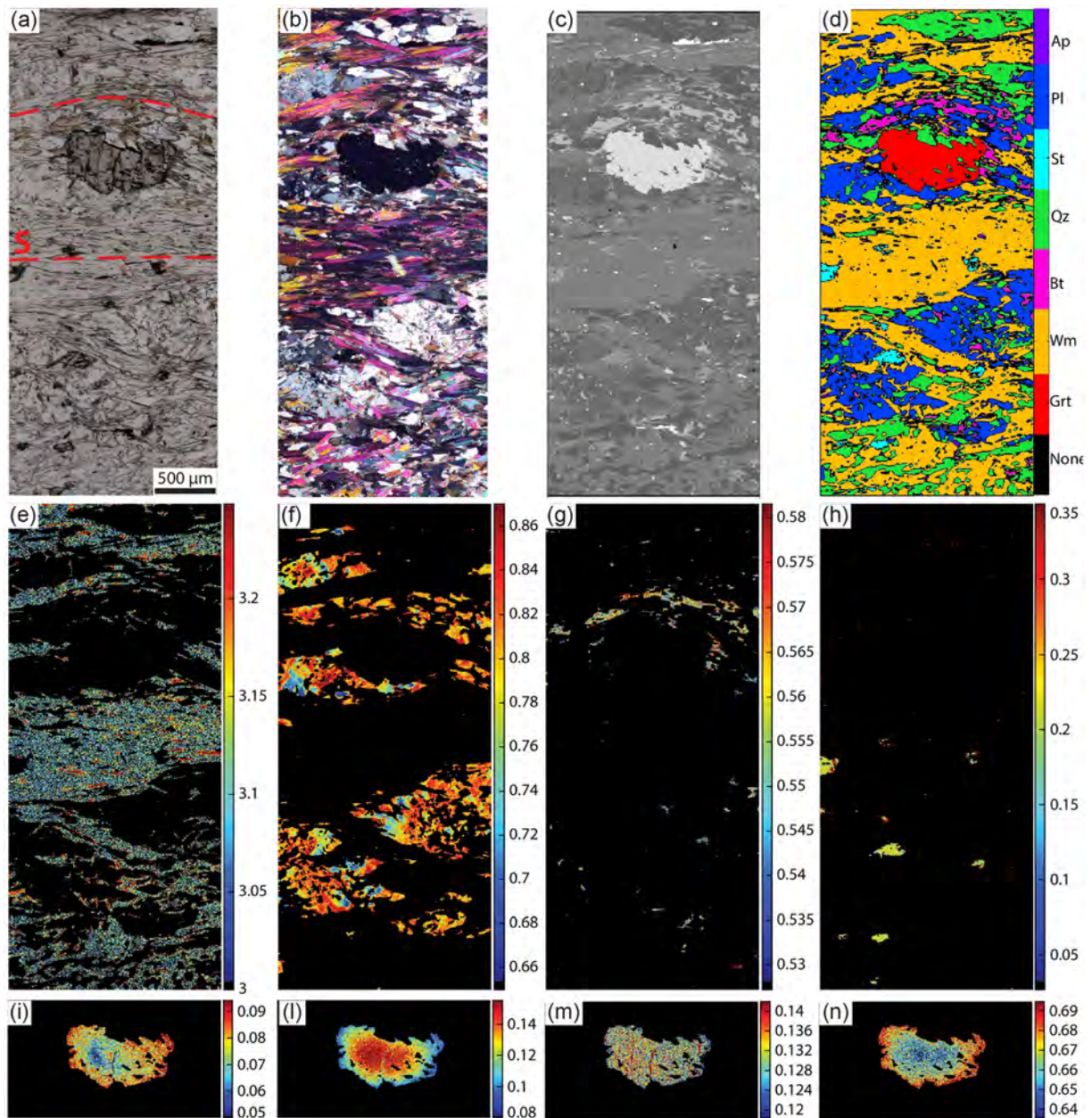


**Figure 9.** Microstructure and chemical data of micaschist Sample 561. (a, b) Optical photo, plane-polarized, and crossed-polarized light, respectively. (c) BSE image. (d–n) Standardized X-ray maps. (d) Map of the mineral phases showing the main foliation defined by muscovite, biotite, staurolite, and plagioclase. (e) Muscovite Si apfu map highlights relic phengitic cores (high in Si apfu) and syn-kinematic rims. (f) Plagioclase  $X_{Ab}$  map displays complex growth zones, with low  $X_{Ab}$  cores and high  $X_{Ab}$  rims. (g) Biotite  $X_{Mg}$  map. (h) Staurolite  $X_{Mg}$  map. (i–n) Garnet  $X_{Grs}$ ,  $X_{Sps}$ ,  $X_{Prp}$ , and  $X_{Alm}$  maps, respectively, display a concentric zoning except for the  $X_{Prp}$  that is more homogeneous.

by a plagioclase richer in albite content. Amphibole  $X_{Mg}$  map highlighting a richer  $X_{Mg}$  relic core and a poorer syn-kinematic rim (Figures 6f and 7e). In Sample 531 thermometric estimates for the plagioclase rim and amphibole rim pairs yield  $610^{\circ}\text{C}$  ( $\pm 50^{\circ}\text{C}$ ) for 0.77 GPa and 0.87 GPa ( $\pm 0.2$  GPa; Bhadra & Bhattacharya, 2007, and Anderson & Smith, 1995, barometers, respectively). In Sample 543 plagioclase rim and amphibole rim pairs yield  $650^{\circ}\text{C}$  for 0.40 GPa and 0.84 GPa (Table 1; see section 5.1 for discussion).

#### 4.2.3. Chlorite and White Mica Multiequilibrium

The chlorite and white mica multiequilibrium technique was used to constrain the equilibrium conditions of chlorite and white mica grains that developed on localized C- and C'-type shear bands that deflect the main foliation. Chlorite and white mica couples crystallizing along C' planes (Sample 640) and C planes (Sample

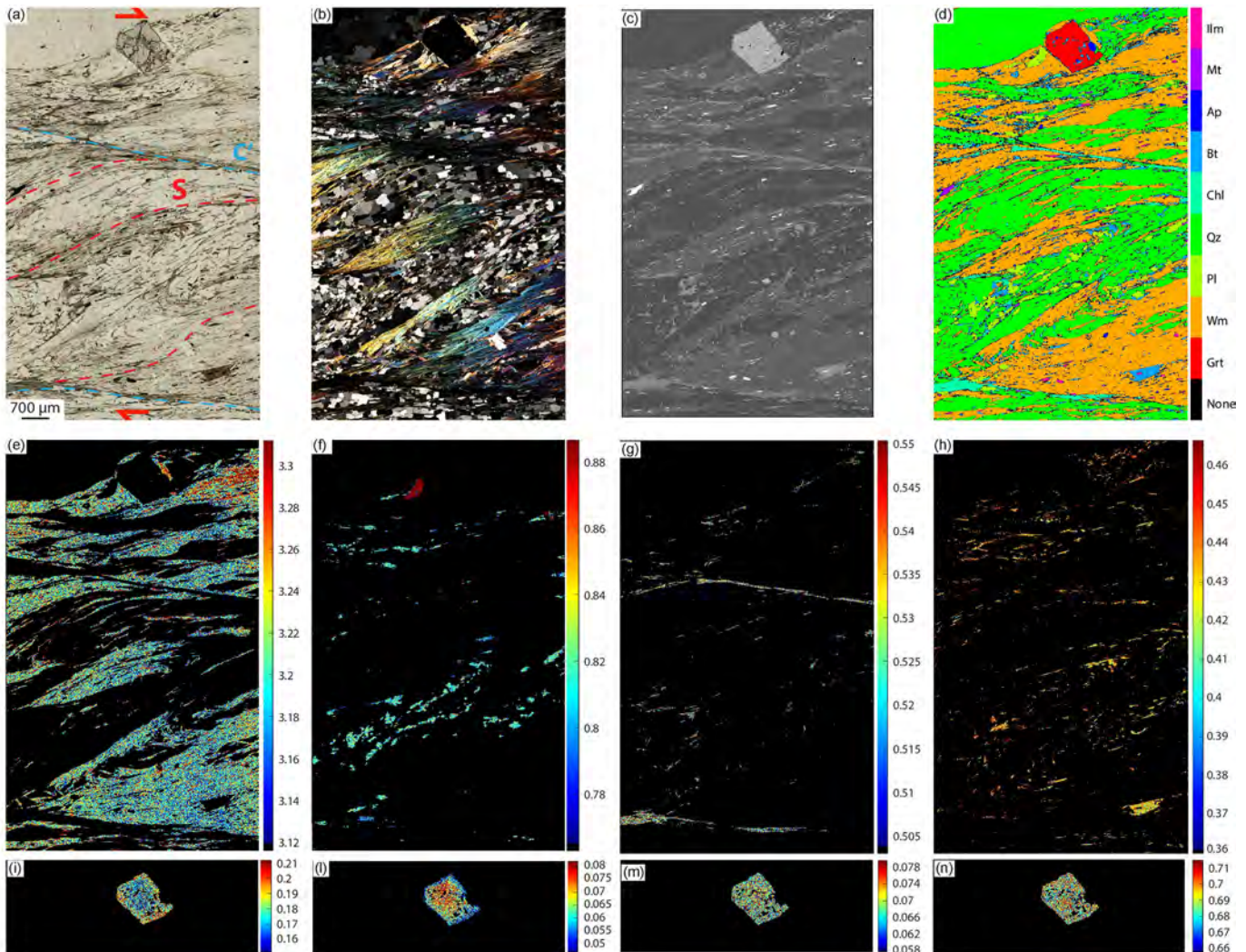


**Figure 10.** Microstructure and chemical data of micaschist Sample 640. (a, b) Optical photo highlighting the amphibolite facies main foliation overprinted by  $C'$  shear bands with a dextral sense of shear, plane-polarized, and crossed-polarized light, respectively. (c) BSE image. (d–n) Standardized X-ray maps. (d) Map of the mineral phases showing the main foliation defined by muscovite and biotite with a sigmoidal shape.  $C'$  shear bands are defined by chlorite and minor muscovite. (e) Muscovite Si apfu map highlights relic phengitic cores (high in Si apfu) and syn-amphibolite facies foliation rims. (f) Plagioclase  $X_{Ab}$  map. (g) Chlorite  $X_{Mg}$  map; note its preferential location along the  $C'$  shear bands. (h) Biotite  $X_{Mg}$  map. (i–n) Garnet  $X_{GrS}$ ,  $X_{SPs}$ ,  $X_{Prp}$ , and  $X_{Alm}$  maps, respectively, display a concentric zoning except for the  $X_{Prp}$  and  $X_{Alm}$  that are more homogeneous.

695) equilibrated at the same pressure conditions of  $0.3 \pm 0.2$  GPa for temperature of  $310 \pm 50^\circ\text{C}$  and  $370 \pm 50^\circ\text{C}$ , respectively (Figure 13 and red dashed rectangles in Figure 12).

#### 4.2.4. Summary of P-T Results

The three micaschist samples record a similar P-T evolution that is characterized by three metamorphic stages. The first HP stage is constrained between  $400^\circ\text{C}$  and  $500^\circ\text{C}$  and 1–1.3 GPa by the chemical composition of phengitic muscovite cores in all the samples, plus garnet and albite cores in Sample 695 ( $M_{HP}$  in Figure 13c). These mineral phases are not associated with any obvious HP foliation and are wrapped by the main mylonitic S foliation developed during the second stage. The mylonitic foliation is the main fabric throughout the middle and lower portion of the drill core, for a depth of  $\sim 1$  km. It formed between  $450$ – $550^\circ\text{C}$  and  $0.5$ – $0.8$  GPa as constrained by muscovite rims and biotite, plus garnet and plagioclase in Samples 561 and 640 ( $M_{Amp}$  in micaschists). In amphibolite Samples 531 and 543, amphibole-plagioclase thermobarometry constrains the development of the mylonitic foliation to  $600$ – $650^\circ\text{C}$  and 0.8 GPa ( $M_{Amp}$  in amphibolites; Table 1; see section 5.1 for discussion). The third stage corresponds to the C and  $C'$  planes, which deform the mylonitic foliation. These planes are present only in deepest Samples 640 and 695 and are most pervasive in

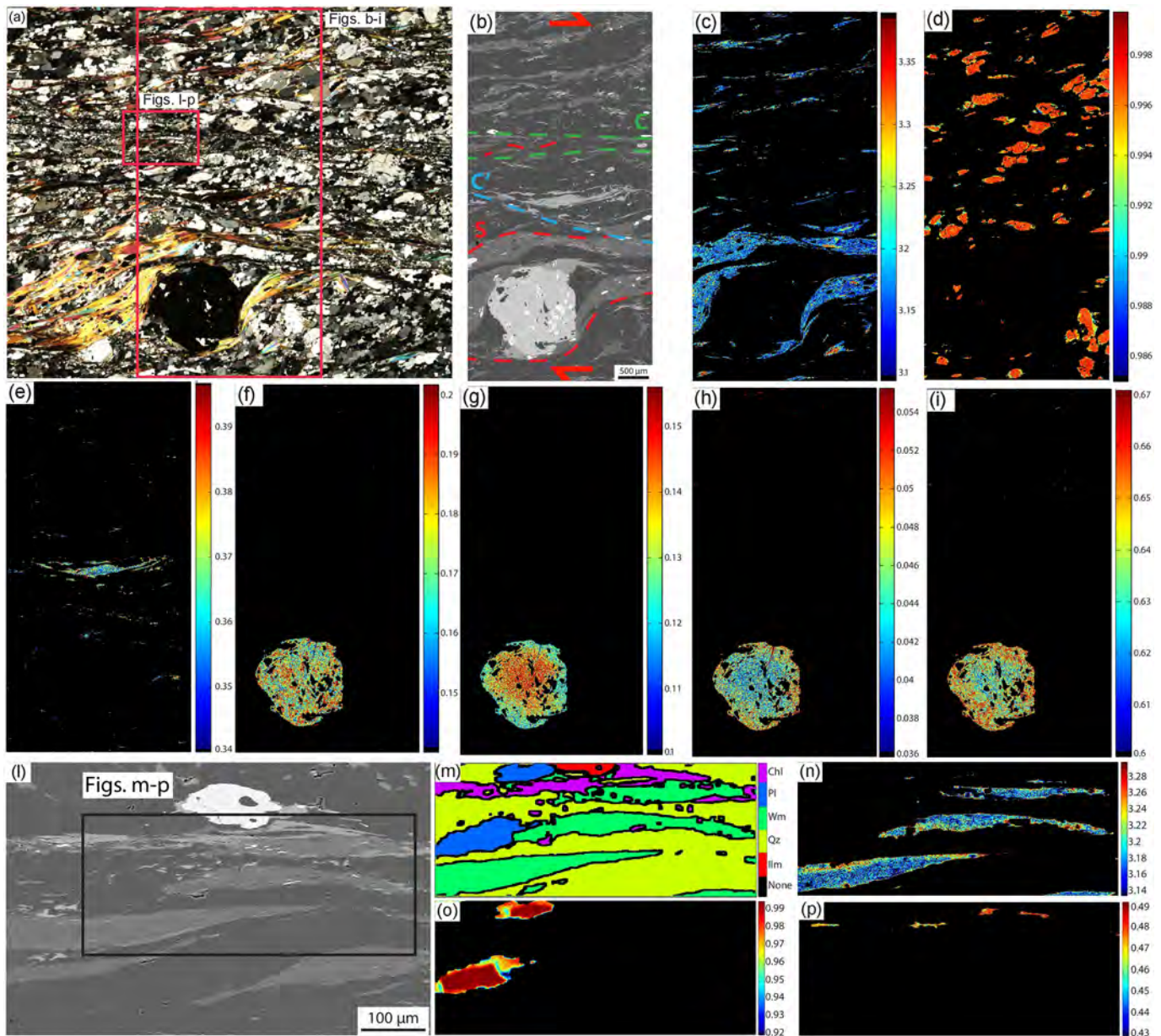


**Figure 11.** Microstructure and chemical data of micaschist Sample 695. (a) Optical photo, crossed-polarized light. (b) BSE image highlighting the main foliation with a dextral sense of shear. (c–i) Standardized X-ray maps. (c) Muscovite Si apfu map highlights relic phengitic cores (high in Si apfu) and syn-kinematic rims. (d) Plagioclase  $X_{Ab}$  map displays high  $X_{Ab}$  cores and lower  $X_{Ab}$  syn-kinematic rims. (e) Biotite  $X_{Mg}$  map. (f–i) Garnet  $X_{GrS}$ ,  $X_{SpS}$ ,  $X_{Prp}$ , and  $X_{Alm}$  maps, respectively, display a concentric zoning except for the  $X_{GrS}$  that is more homogeneous. (l) BSE image of C-type shear bands defined mainly by chlorite and minor muscovite. (m–p) Standardized X-ray maps. (m) Map of the mineral phases. (n) Muscovite Si apfu map. (o) Plagioclase  $X_{Ab}$  map. (p) Chlorite  $X_{Mg}$  map.

the latter. Model results based on the chemistry of chlorite and muscovite grains in textural equilibrium growing along such structures suggest P–T conditions of equilibration at  $\sim 0.3$  GPa for temperature conditions of 300–350°C ( $M_{Gr}$  in Figure 13c).

### 4.3. EBSD Analysis

#### 4.3.1. Micaschists

In Sample 640, the EBSD analysis was performed on a domain where the  $C'$  planes are well developed, in order to provide insight into the deformation mechanisms responsible for forming these structures. This domain consists of monomineralic quartz layers separated by thin ( $\sim 10$   $\mu\text{m}$  thick) discontinuous bands of muscovite and chlorite (Figure 14). Quartz average grain size is 30  $\mu\text{m}$ , with maximum value of  $\sim 150$   $\mu\text{m}$ .

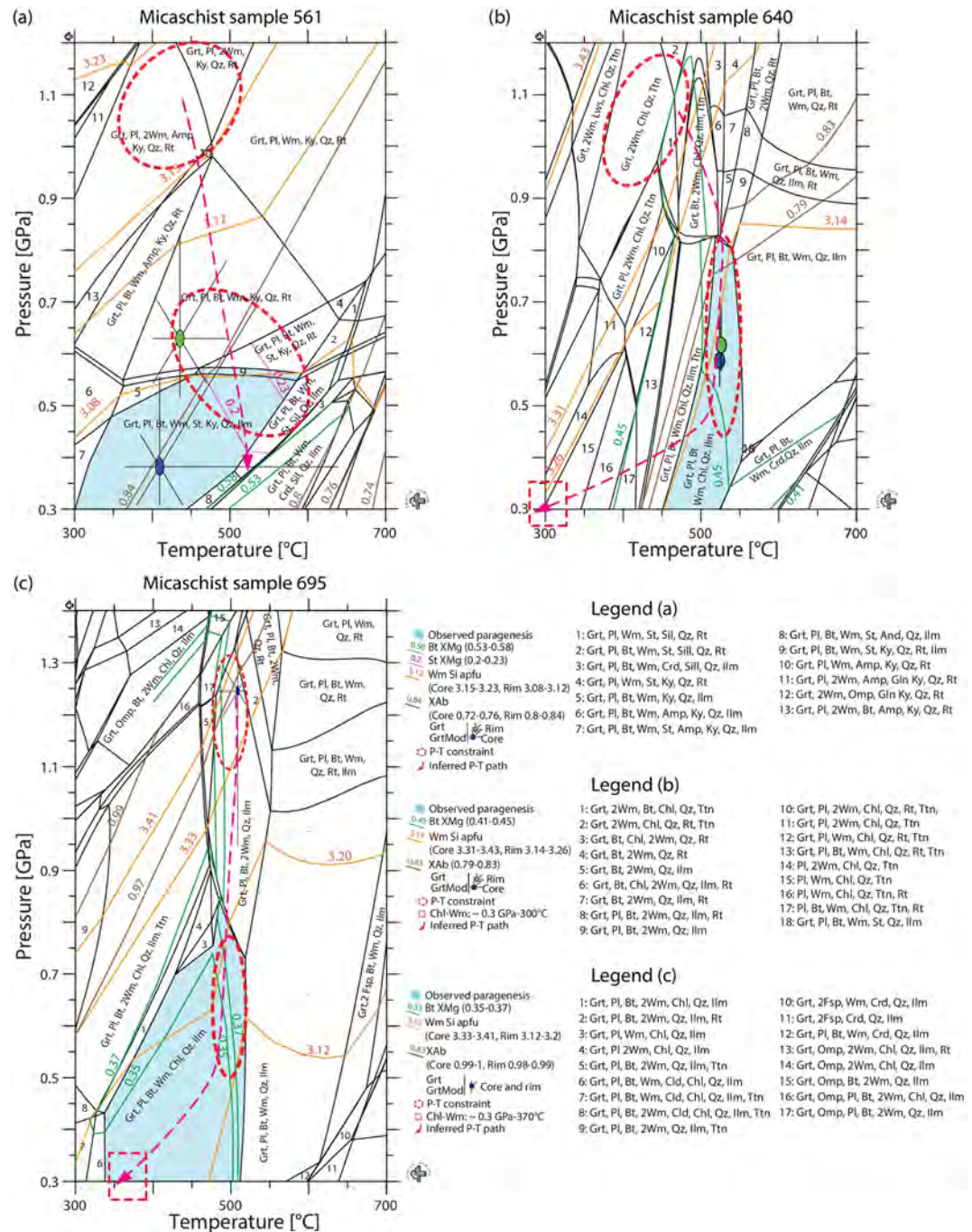


**Figure 12.** (a–c) Equilibrium phase diagrams of the micaschists samples computed with Theriak-Domino (de Capitani & Petrakakis, 2010) with plotted chlorite and white mica multi-equilibrium results. The error bars departing from filled ellipses show the P-T uncertainties related to the analytical error of the garnet compositions. Red dashed ellipses indicate the P-T conditions of the metamorphic stages best fitting with the observed paragenesis and the computed isopleths. Red dashed rectangles indicate the Chlorite + white mica + quartz + H<sub>2</sub>O thermobarometry results. Purple dashed lines represent the inferred P-T paths for each specific sample. See text for discussion.

Quartz grains display undulose extinction, lobate grain boundaries, and several low-angle boundaries. Smaller grains with grain size between 20 and 40 μm are evident at the boundaries of larger grains (Figure 14c). GOS values vary from <1° (generally in the smaller grains) to maximum values of ~7° (generally in the larger grains; Figure 14b). Pole figures show a well-defined crystallographic-preferred orientation (CPO) of the *c* axis forming a short girdle slightly inclined to the YZ plane (Figure 14e). The



**Table 1**  
*Results of Amphibole-Plagioclase Geothermobarometry*

Amp-Pl couples	Thermometer HB	Barometer	
		BB	AS
531AmpRim-PlRim	<b>610°C</b>	<b>0.77 GPa</b>	0.87 GPa
543AmpRim-PlRim	<b>651°C</b>	0.40 GPa	<b>0.84 GPa</b>

*Note.* Thermometer abbreviation: HB = Holland and Blundy (1994). Barometer abbreviations: BB = Bhadra and Bhattacharya (2007); AS = Anderson and Smith (1995). The favored results are highlighted in bold (see discussion section for details).

misorientation angle distribution of both correlated and uncorrelated pairs shows peaks at low angle misorientations (between 2° and 10°) and, for correlated misorientations, at around 60°, related to the Dauphiné twinning (Figure 14d; Lloyd, 2004; Menegon et al., 2011). The plots of misorientation axis in crystal coordinates for misorientations of 2–10° display a major cluster around the *c* axis (Figure 14e).

In Sample 695 the investigated monomineralic quartz layers occur along the mylonitic S foliation and are separated by C planes defined by chlorite and muscovite grains. A bigger muscovite crystal with a sigmoidal shape is dragged into a C plane, defining a dextral sense of shear consistent with the geometry of the S-C fabric. This domain was subdivided into four sub-

sets based on the abrupt decrease of quartz grain size from the S foliation to the C planes. Subsets 1 and 2 were sampled along the S foliation, whereas Subsets 3 and 4 were sampled along C planes (Figure 15). In Subsets 1 and 2 the quartz average grain size is 36 and 10 μm, respectively, with maximum value of 150 μm in the former (Figure 15d). Quartz grains display undulose extinction, lobate grain boundaries, and several low-angle boundaries. GOS values vary from <1.5° (generally in grains smaller than 50 μm) to maximum values of ~7.5° (Figure 15c). Subset 1 pole figure shows a strong CPO of the *c* axis forming a short girdle along the YZ plane centered on the Y direction (Figure 16a). Subset 2 display a *c*-axis distribution forming a short girdle at 45° to the YZ plane, synthetically inclined with the dextral sense of shear (Figure 16b). The misorientation angle distributions of both correlated and uncorrelated pairs of the two subsets show strong peaks at low angle misorientations (between 2° and 10°) and, for correlated misorientations, at around 60°. Minor peaks are evident for values between 22° and 42° for uncorrelated pairs in Subset 1. The plots of misorientation axis in crystal coordinates for misorientations of 2–10° of Subsets 1 and 2 display a major cluster around the *c* axis.

Both Subsets 3 and 4 display an average grain size of ~5 μm. In Subset 3 a decrease in grain size is visible moving toward the C plane and varies between 1.5 and 6 μm (Figure 15d). GOS values are related to the grain size, with values up to 4.5° in the bigger grains and <1° in the smaller grains (Figure 15c). For these two subsets no obvious CPO is evident in the pole figures (Figures 16c and 16d). The misorientation angle distributions of both correlated and uncorrelated pairs of the two subsets show strong peaks at low angle misorientations (between 2° and 10°), with higher values in Subset 3 for correlated pairs, and for correlated misorientations at around 60°. The plots of misorientation axis in crystal coordinates for misorientations of 2–10° do not show any obvious cluster, although the limited amount of data points (especially for Subset 4) does not allow to draw solid conclusions. Although the number of grains in our data set is too small to perform solid statistical analysis of grain and subgrain size, we note that subgrains within Subset 1 are generally much bigger than those in Subsets 2 and 3.

In both samples, muscovite and chlorite display a strong CPO with the poles of the (001) parallel to Z, and with the poles of (100) and (010) defining girdles lying on the XY plane (Figure S1). In particular, in Sample 695 the asymmetry of the (001) maximum of muscovite confirms the dextral sense of shear (Dempsey et al., 2011).

#### 4.3.2. Titanite Grains in Amphibolites

In Sample 531 we investigated a pressure shadow between two sigmoidal plagioclase porphyroclasts composed of ilmenite grains rimmed by titanite, and a single grain of titanite elongated parallel to the mylonitic foliation (Figures 6 and 8, respectively; see section 4.1.2). Titanite is characterized by GOS values lower than 4°, with several grains displaying values lower than 1° (Figures 8c–8g). The GOS values are related to the grain size, with the higher values found in larger grains. Titanite displays a weak CPO, with the (100) and [001] subparallel to the foliation and to the stretching lineation, respectively (Figure 8i).

#### 4.4. U-Pb Geochronology

Analyzed titanite grains in amphibolite Samples 531, 543, and 557 contained U concentrations of ~3 to 12, ~4 to 33, and ~1 to 15 ppm, respectively (Table S3). Common-Pb-uncorrected data, plotted on Tera-Wasserburg diagrams (Figure 17), yield  $^{238}\text{U}/^{206}\text{Pb}$ – $^{207}\text{Pb}/^{206}\text{Pb}$  isochrons with lower intercept dates of  $429 \pm 20$  Ma (95% confidence interval with overdispersion; mean square of weighted deviation MSWD = 2.6),  $417 \pm 9$  Ma (MSWD = 1.2), and  $461 \pm 21$  Ma (MSWD = 1.5) in Samples 531, 543, and 557, respectively. The  $^{207}\text{Pb}/$

**Table 2**  
Representative Average Composition Analysis (wt%) of Garnet, Muscovite, Biotite, and Staurolite.

Sample	Grt												Ph-Ms						Bt		St
	561			640A			695			561			640A			561	640A	695	561		
	CORE	RIM	561	CORE	RIM	640A	CORE	RIM	695	CORE	RIM	561	CORE	RIM	640A	CORE	RIM	695	C planes	C planes	
SiO <sub>2</sub>	36.23	36.80	36.97	37.09	36.94	36.94	49.17	47.22	50.24	46.16	46.02	51.56	48.16	47.15	36.39	36.58	35.27	28.96			
TiO <sub>2</sub>	0.07	0.07	0.05	0.05	0.11	0.11	0.42	0.47	0.30	0.35	0.30	0.24	0.32	0.39	1.61	2.12	1.80	0.49			
Al <sub>2</sub> O <sub>3</sub>	21.06	21.33	20.79	20.86	21.20	21.17	32.43	35.20	28.72	31.05	31.93	28.86	33.34	31.33	18.10	17.89	17.22	53.36			
FeO	29.44	31.28	30.80	31.12	28.44	29.26	2.27	1.98	2.84	2.88	2.67	3.93	3.02	4.25	17.09	20.62	24.51	12.54			
MnO	6.85	4.51	3.06	2.56	6.42	5.56	0.01	0.01	0.02	0.02	0.01	0.01	0.01	0.01	0.05	0.01	0.10	0.26			
MgO	3.38	3.27	1.75	1.72	1.09	1.22	1.50	0.73	2.09	1.20	0.96	2.38	1.13	1.64	12.14	8.81	7.72	1.91			
CaO	2.06	3.17	6.31	6.60	6.27	6.28	0.01	0.01	0.03	0.03	0.03	0.01	0.01	0.01	0.01	0.01	0.06	0.01			
Na <sub>2</sub> O	—	—	—	—	—	—	1.61	2.17	0.75	1.07	1.27	0.65	1.12	0.56	0.39	0.20	0.09	0.04			
K <sub>2</sub> O	—	—	—	—	—	—	9.21	8.56	10.05	9.91	9.63	10.09	9.77	10.43	9.33	9.56	8.92	0.00			
Total	99.08	100.42	99.72	100.00	100.48	100.53	96.63	96.35	95.04	92.66	92.82	97.72	96.87	95.77	95.09	95.80	95.68	97.56			
Formulae based on 12 O																					
Si	2.93	2.94	2.98	2.98	2.97	2.98	3.22	3.10	3.36	3.19	3.16	3.37	3.17	3.17	2.74	2.78	2.74	4.00			
Ti	0.00	0.00	0.00	0.00	0.01	0.01	0.02	0.02	0.01	0.02	0.02	0.01	0.02	0.02	0.09	0.12	0.10	0.05			
Al	2.01	2.01	1.98	1.98	2.01	2.01	2.50	2.72	2.26	2.53	2.59	2.22	2.58	2.48	1.61	1.60	1.58	8.68			
Fe	2.00	2.09	2.08	2.09	1.91	1.97	0.12	0.11	0.16	0.17	0.15	0.21	0.17	0.24	1.08	1.31	1.59	1.45			
Mn	0.47	0.30	0.21	0.17	0.44	0.35	0.00	0.00	0.00	0.00	0.00	0.00	0.00	0.00	0.00	0.00	0.01	0.03			
Mg	0.41	0.39	0.21	0.21	0.13	0.15	0.15	0.07	0.21	0.12	0.10	0.23	0.11	0.16	1.36	1.00	0.89	0.39			
Ca	0.18	0.27	0.54	0.57	0.54	0.54	0.00	0.00	0.00	0.00	0.00	0.00	0.00	0.00	0.00	0.00	0.00	0.00			
Na	—	—	—	—	—	—	0.20	0.28	0.10	0.14	0.17	0.08	0.14	0.07	0.06	0.03	0.01	0.01			
K	—	—	—	—	—	—	0.77	0.72	0.86	0.87	0.84	0.84	0.82	0.90	0.90	0.93	0.88	0.00			
∑ cations	8.01	8.00	8.00	8.00	8.00	8.00	6.99	7.02	6.97	7.04	7.03	6.97	7.01	7.05	7.84	7.77	7.82	14.61			
X <sub>Mg</sub>	—	—	—	—	—	—	0.54	0.40	0.57	0.43	0.39	0.52	0.40	0.41	0.56	0.43	0.36	0.21			
Molecular proportions of garnet end members																					
Alm	0.65	0.68	0.68	0.69	0.63	0.65	—	—	—	—	—	—	—	—	—	—	—	—			
Prp	0.13	0.13	0.07	0.07	0.04	0.05	—	—	—	—	—	—	—	—	—	—	—	—			
Grs	0.06	0.09	0.18	0.19	0.18	0.18	—	—	—	—	—	—	—	—	—	—	—	—			
Sps	0.15	0.10	0.07	0.06	0.15	0.13	—	—	—	—	—	—	—	—	—	—	—	—			

**Table 3**  
Representative Average Composition and Spot Analysis (wt%) of Plagioclase, Amphibole, and Chlorite

Sample	Pl										Amp				Chl	
	561		640A		695		531		543		531		543		640A	695
	CORE	RIM	CORE	RIM	CORE	RIM	CORE	RIM	CORE	RIM	CORE	RIM	CORE	RIM		Spot analysis
Average composition (wt%)																
SiO <sub>2</sub>	62.56	64.01	63.73	67.03	69.11	66.28	59.69	62.23	59.68	62.25	52.55	44.55	47.73	42.54	25.19	24.44
TiO <sub>2</sub>	0.01	0.01	0.02	0.02	0.01	0.01	0.02	0.02	0.02	0.02	0.28	0.35	0.50	0.38	0.13	0.21
Al <sub>2</sub> O <sub>3</sub>	25.28	24.05	22.48	19.68	20.28	22.74	25.75	24.07	25.06	23.33	4.40	13.52	9.57	13.39	21.01	20.95
FeO	0.06	0.06	0.06	0.04	0.05	0.06	0.07	0.10	0.11	0.14	12.56	15.55	13.49	15.94	25.73	30.95
MnO	0.01	0.01	0.01	0.01	0.03	0.03	0.02	0.02	0.01	0.01	0.22	0.22	0.23	0.25	0.06	0.21
MgO	0.00	0.00	0.00	0.00	0.00	0.00	0.01	0.01	0.01	0.01	15.42	10.25	12.62	10.49	12.84	11.35
CaO	5.47	4.06	3.95	0.17	0.01	0.10	7.02	4.10	6.67	4.33	12.07	11.82	11.40	11.70	0.01	0.00
Na <sub>2</sub> O	9.22	10.09	9.75	12.06	13.09	11.19	8.02	9.74	8.49	9.92	0.70	1.77	1.67	2.15	0.01	0.00
K <sub>2</sub> O	0.05	0.04	0.09	0.08	0.06	0.18	0.06	0.05	0.04	0.04	0.11	0.30	0.21	0.31	0.55	0.06
Sum	102.64	102.33	100.08	99.09	102.63	100.60	100.65	100.32	100.09	100.04	98.32	98.34	97.43	97.16	85.52	88.17
	Formulae based on 8 O										on 23 anhydrous O				on 14 anhydrous O	
Si	2.71	2.77	2.82	2.97	2.96	2.88	2.65	2.75	2.66	2.76	7.48	6.49	6.92	6.31	2.72	2.65
Ti	—	—	—	—	—	—	—	—	—	—	0.03	0.04	0.05	0.04	—	—
Al	1.29	1.23	1.17	1.03	1.02	1.17	1.35	1.25	1.32	1.22	0.74	2.32	1.64	2.34	2.69	2.67
Fe <sup>3+</sup>	—	—	—	—	—	—	—	—	—	—	0.25	0.36	0.36	0.55	0.06	0.00
Fe <sup>2+</sup>	—	—	—	—	—	—	—	—	—	—	1.20	1.53	1.28	1.42	2.27	2.80
Mn	—	—	—	—	—	—	—	—	—	—	0.03	0.03	0.03	0.03	—	—
Mg	—	—	—	—	—	—	—	—	—	—	3.27	2.23	2.73	2.32	2.07	1.83
Ca	0.25	0.19	0.19	0.01	0.00	0.01	0.33	0.19	0.32	0.21	1.84	1.85	1.77	1.86	—	—
Na	0.77	0.85	0.84	1.03	1.09	0.94	0.69	0.83	0.74	0.85	0.20	0.51	0.47	0.63	—	—
K	0.05	0.00	0.01	0.00	0.00	0.02	0.00	0.00	0.00	0.00	0.02	0.06	0.04	0.06	—	—
Sum	5.08	5.04	5.01	5.04	5.07	5.01	5.02	5.04	5.04	5.05	15.06	15.41	15.28	15.54	9.81	9.95
X <sub>Mg</sub>	—	—	—	—	—	—	—	—	—	—	0.69	0.54	0.63	0.54	0.47	0.40
X <sub>Ab</sub>	0.75	0.82	0.81	0.99	1.00	0.98	0.67	0.81	0.70	0.80	—	—	—	—	—	—
X <sub>An</sub>	0.25	0.18	0.18	0.01	0.00	0.01	0.33	0.19	0.30	0.19	—	—	—	—	—	—

<sup>206</sup>Pb ratios of common Pb incorporated into the titanite (taken from y intercepts on Tera-Wasserburg concordia diagrams) are within uncertainty for Samples 531 and 543 ( $0.816 \pm 0.026$  and  $0.812 \pm 0.019$ , respectively). Sample 557 shows higher <sup>207</sup>Pb/<sup>206</sup>Pb ratio of common Pb ( $0.933 \pm 0.020$ ) compared to the two other samples.

## 5. Discussion

### 5.1. P-T-t Conditions of Metamorphism and Deformation

The pressure estimates calculated for amphibolite Samples 531 and 543 are within error of each other for the two geobarometer calibrations (Table 1). However, the pressure calculated for Sample 543 using the Bhadra and Bhattacharya (2007) geobarometer deviates by 0.4 GPa compared to the Anderson and Smith (1995) geobarometer. We suggest that the latter estimate is more reliable, as it lies within error of the results calculated for Sample 531. Moreover, Sample 531 was collected from a few tens of meters above 543, and it is characterized by the same fabrics and similar mineralogy. These data match the results of amphibolite Sample 648 collected from ~1,000 m deeper in the drill core (Giuntoli, Menegon, & Warren, 2018), suggesting that the evolution of the mylonitic foliation in the amphibolites is consistent through middle and lower portions of the drill core. Notably, amphibolite Sample 648 of Giuntoli, Menegon, and Warren (2018) recorded higher P conditions, up to 1 GPa, linked to the incipient stage of the mylonitic foliation development. In the same sample, chlorite-rich C' planes yielded T of 350–200°C using the Chlorite + Quartz + H<sub>2</sub>O thermometry. These temperature results match with the conditions estimated for the C and C' planes in the micaschist samples (M<sub>Gr</sub>; Figure 13).

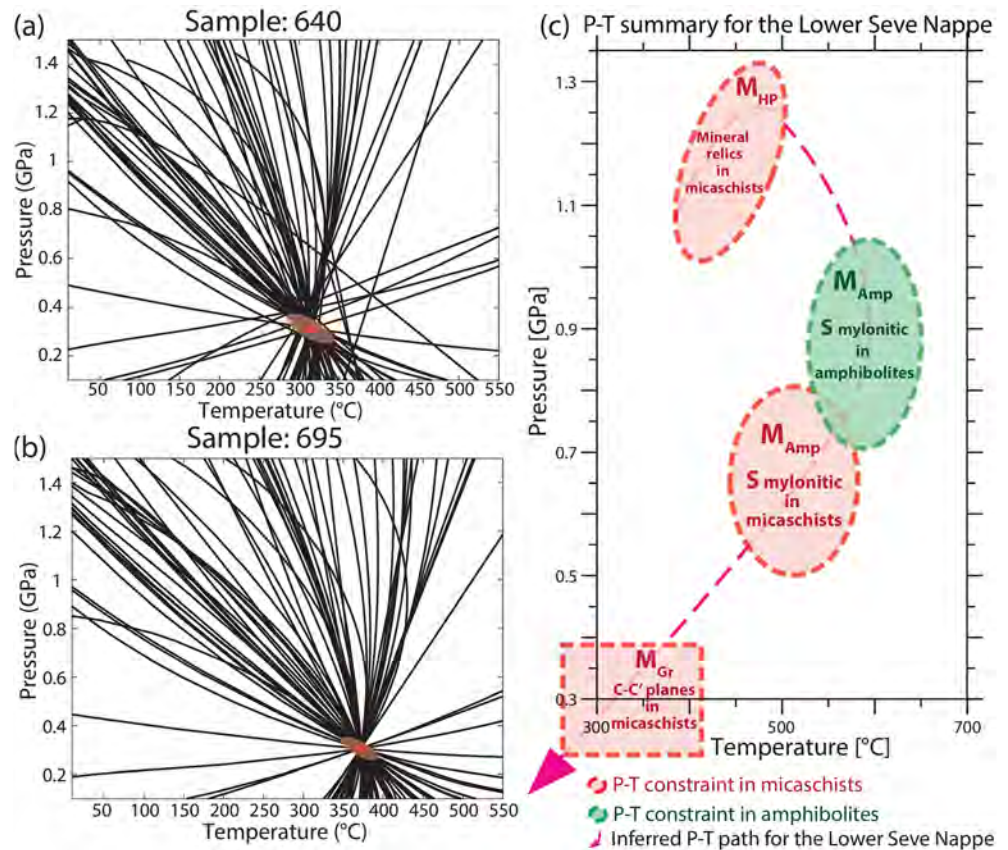


**Figure 13.** (a, b) Chlorite + white mica + quartz + H<sub>2</sub>O thermobarometry results; the red ellipses represent the P-T uncertainties. (c) P-T summary path of the studied samples with highlighted the three metamorphic stages described in the text ( $M_{HP}$ ,  $M_{Amp}$ , and  $M_{Gr}$ ).

The temperature estimates suggest a difference of 50–100°C between the mylonitic foliation ( $M_{Amp}$ ) in the micaschists and the amphibolite. This  $\Delta T$  could be either related to the two different methods used to constrain P and T conditions in the micaschists (isochemical phase diagrams; section 4.2.1) and in the amphibolites (amphibole-plagioclase thermobarometry; section 4.2.2) or to re-equilibration of the micaschists at decreasing T during the development of the mylonitic foliation. Plagioclase core  $X_{Ab}$  isopleths in Sample 561 also suggest a higher-temperature (~650°) stage (Figure 12a), although no other evidence for higher temperatures is (now) recorded by the studied micaschist samples. We disregard the possibility that those two lithotypes were juxtaposed only after their temperature peak, thus experiencing different tectonometamorphic histories, as intercalated micaschist and amphibolite samples were collected along the drill core (Figure 2; see section 5.3 for further discussion).

Titanite U-Pb geochronology of amphibolite Sample 543 yields a simple isochron that we interpret to reflect formation of the mylonitic foliation at  $417 \pm 9$  Ma (MSWD = 1.2; Figure 17). The titanite U-Pb data from Samples 531 and 557 are more complex. Sample 531 yields an isochron with an age that is within uncertainty of both samples ( $429 \pm 20$  Ma; MSWD = 2.6), whereas 557 yields an older age of  $461 \pm 21$  Ma (MSWD = 1.5) and higher  $^{207}\text{Pb}/^{206}\text{Pb}$  ratio compared to the previous samples. In all the analyzed samples, the titanite microstructural data suggest that it formed with the mylonitic S foliation and no evidence of a core to rim growth is present in standardized X-ray maps and BSE images (see section 4.1.2). Therefore, the spread of ages, the large uncertainties, and the relatively high MSWD of regressions in 531 and 557 could reflect the duration of the mylonitic foliation development (from higher temperature and pressure conditions to lower ones; Figure 18), with stages of titanite crystallization related to differences in local bulk compositions, fluid availability, and mineral reactions (Papapavlou et al., 2017; Spencer et al., 2013). Titanite growing over a protracted time range has recently been documented both from other areas in the Caledonides (e.g., Faber et al., 2019; Gasser et al., 2015; Spencer et al., 2013) and in other similar geological settings (e.g., Walters

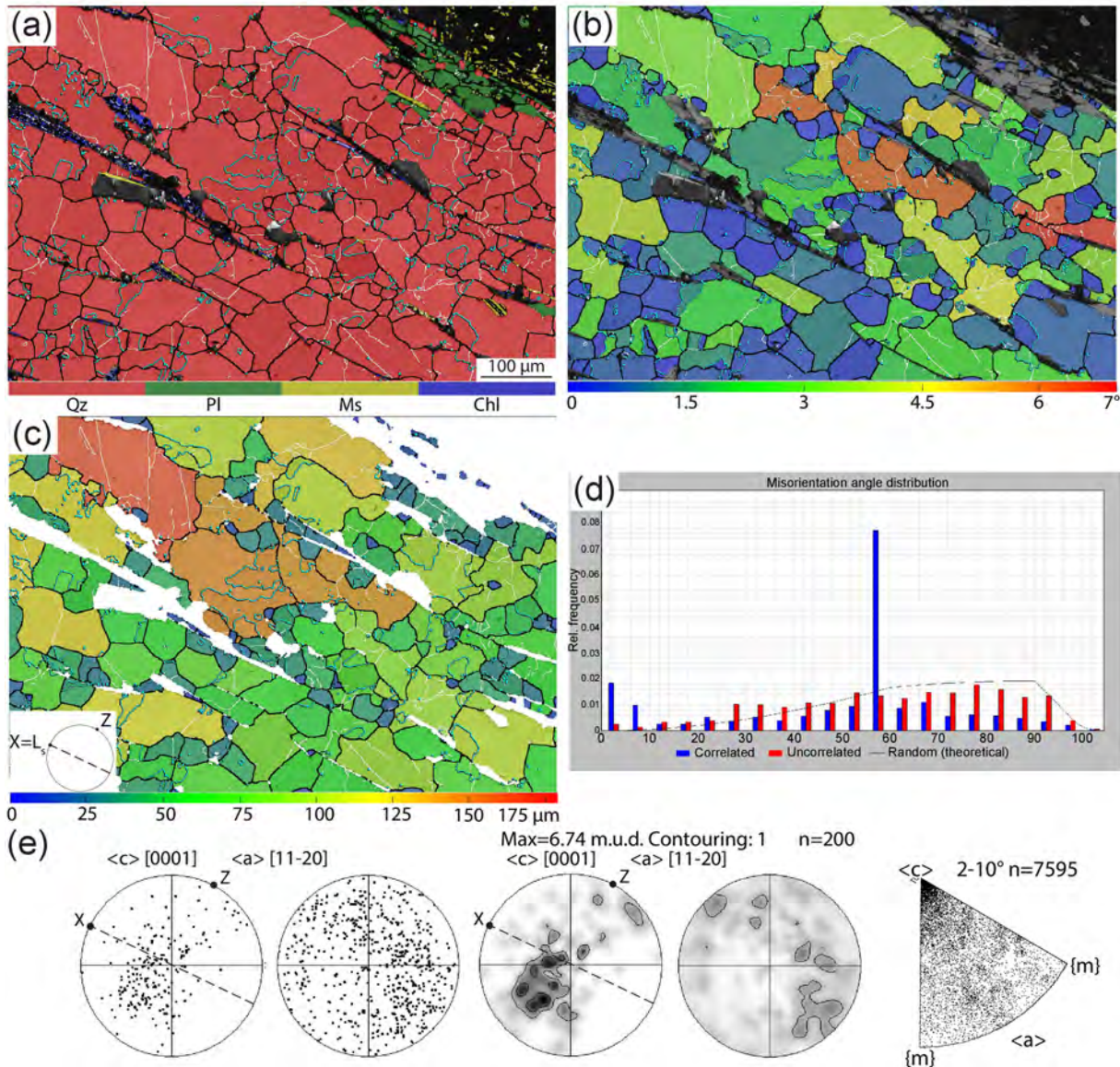


**Figure 14.** EBSD data of the  $C'$  shear band domain in micaschist Sample 640. (a) EBSD phase map. Note the fine-grained chlorite and muscovite growing along the  $C'$  planes. White lines indicate low-angle boundaries ( $2\text{--}10^\circ$ ), black lines high-angle boundaries ( $>10^\circ$ ), and light blue lines Dauphiné twin boundaries in quartz. (b) Quartz GOS map highlights grains with low GOS values at the boundaries of grains with higher GOS values. (c) Quartz grain size map. (d) Misorientation angle distribution of quartz displaying peaks at low angle misorientations and at  $60^\circ$  for correlated pairs. (e) Quartz pole figures of crystallographic axes, and plot of misorientation axis in crystal coordinates associated with low-angle misorientation ( $2\text{--}10^\circ$ ) in quartz. Pole figures plotted on the lower hemisphere of the stereographic projection.  $n$  = number of grains (one point per grain). Half width  $10^\circ$  and cluster size  $5^\circ$ , maximum value is given. Quartz grains display a CPO of the  $c$ -axis forming a short girdle at  $45^\circ$  of the  $YZ$  plane.

& Kohn, 2017). We consider it unlikely that the titanites have experienced diffusional Pb loss during cooling, as the maximum temperature estimated in our samples is  $600\text{--}650^\circ\text{C}$ , lower than the effective closure temperature of titanite (e.g., Hartnady et al., 2019; Kohn, 2017; Spencer et al., 2013). Additionally, titanite was stable during deformation without any evidence of dissolution-precipitation processes (e.g., lobate or peninsular edges, mineral inclusions marking transient porosity; Putnis, 2015), and EBSD data show limited or no evidence of deformation by dislocation creep. As these two deformation mechanisms could affect titanite age dating results, their absence, determined from microstructural observations, further supports our interpretation (Papapavlou et al., 2017; Walters & Kohn, 2017).

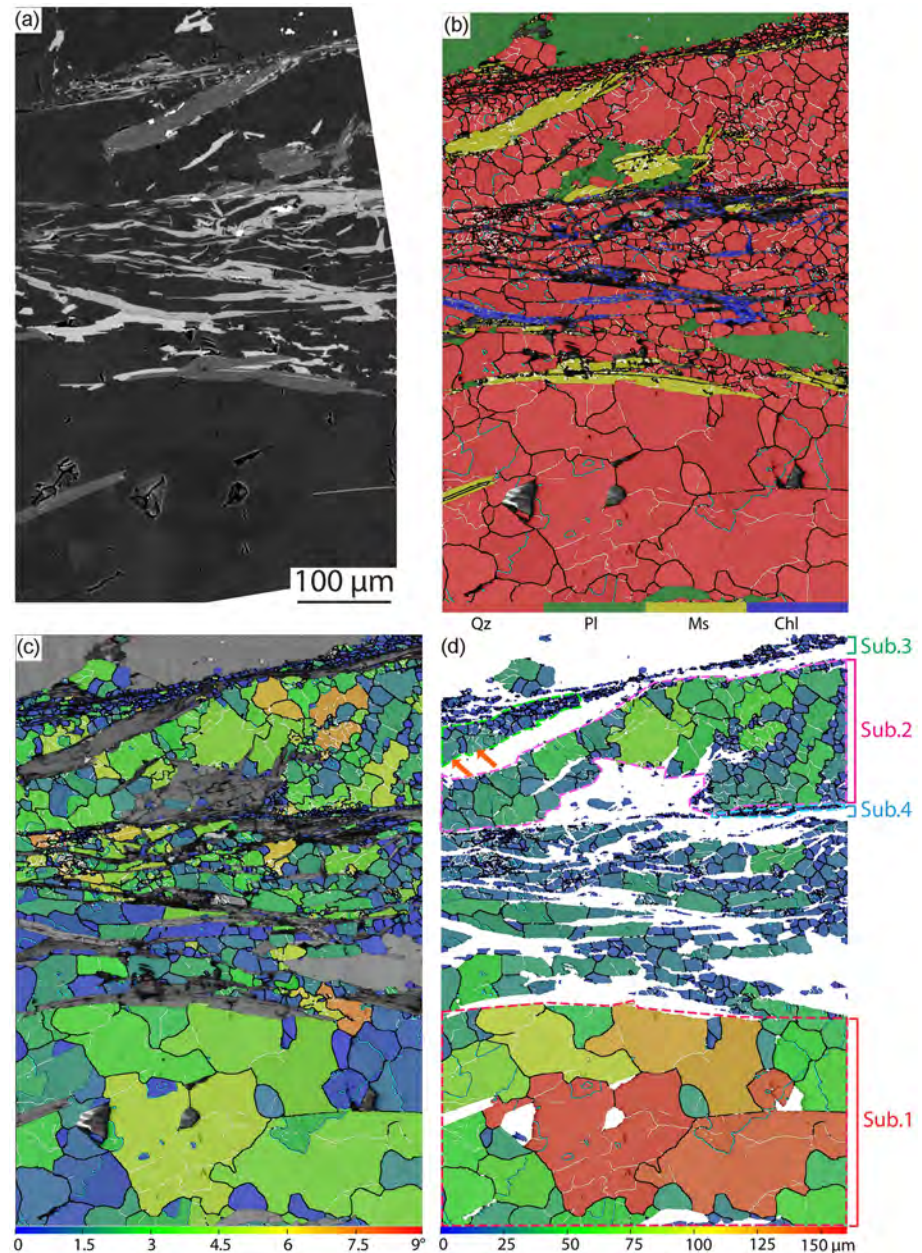


**Figure 15.** Domain with C-type shear bands deforming the mylonitic foliation of micaschist 695 investigated by EBSD. (a, b) BSE image and EBSD phase map highlighting the phyllosilicates crystallizing along the C planes. Note the fine-grained chlorite and muscovite growing along the C planes. The bigger grains of such minerals are reoriented parallel to the C planes. (c) Quartz GOS map highlights that smaller grains have very low internal strain. (d) Quartz grain size map displays grain size reduction in proximity of the C planes. The arrows indicate subgrains forming in the bigger grains (see the text). Subsets 1 to 4 are highlighted with the dashed lines.

### 5.2. Progressive Strain Localization on C'- and C-Type Shear Bands During Protracted Shearing

Micaschist Samples 640 and 695 display a progressive reduction of the recrystallized grain size of quartz in proximity to the C and C' planes (Figure 4). The grain size reduction is more pronounced toward the C planes (Sample 695; Figure 15d). In both samples, the strong peaks at low angle misorientations (between 2° and 10°; Figures 14d and 16) in the misorientation angle distribution are consistent with dynamic recrystallization by subgrain rotation, as adjacent grains formed by subgrain rotation recrystallization display low angular relationships due to crystallographic inheritance from the parental grain (Wheeler et al., 2001). The peak around 60° is associated with Dauphiné twinning (Menegon et al., 2011). Clustering of misorientation

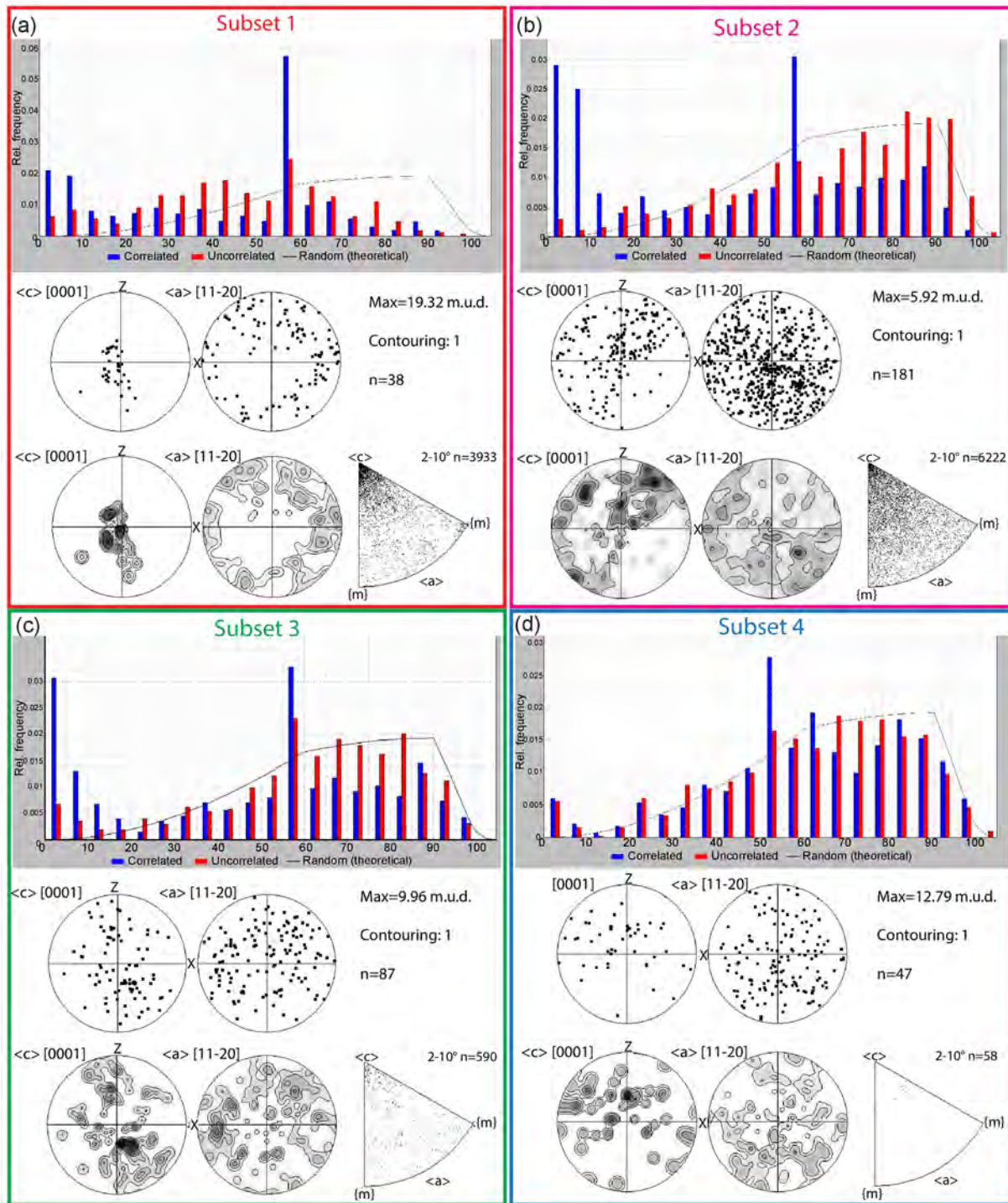


**Figure 16.** Misorientation angle distribution of quartz, pole figures of the crystallographic axes, and plots of misorientation axis in crystal coordinates for the area of micaschist Sample 695 shown in Figure 15. (a–d) Data for quartz from Subset 1–4, respectively, defined in Figure 15d. All subsets show peaks at low angle misorientations and at 60° for both correlated and uncorrelated pairs. Subsets 1 and 2 display CPO and a maximum around  $\langle c \rangle$  in the plot of misorientation axis in crystal coordinates. These features are not present in Subsets 3 and 4.

axes around  $\langle c \rangle$  is consistent with prism  $\langle a \rangle$  slip during recovery and development of tilt boundaries (Neumann, 2000). Furthermore, in micaschist Sample 695 the misorientation angle distribution displays peaks higher than the random distribution up to 30°, compatible with progressive formation of high-angle boundaries due to continuous rotation of subgrains (Neumann, 2000). Quartz  $c$ -axis CPO in micaschist

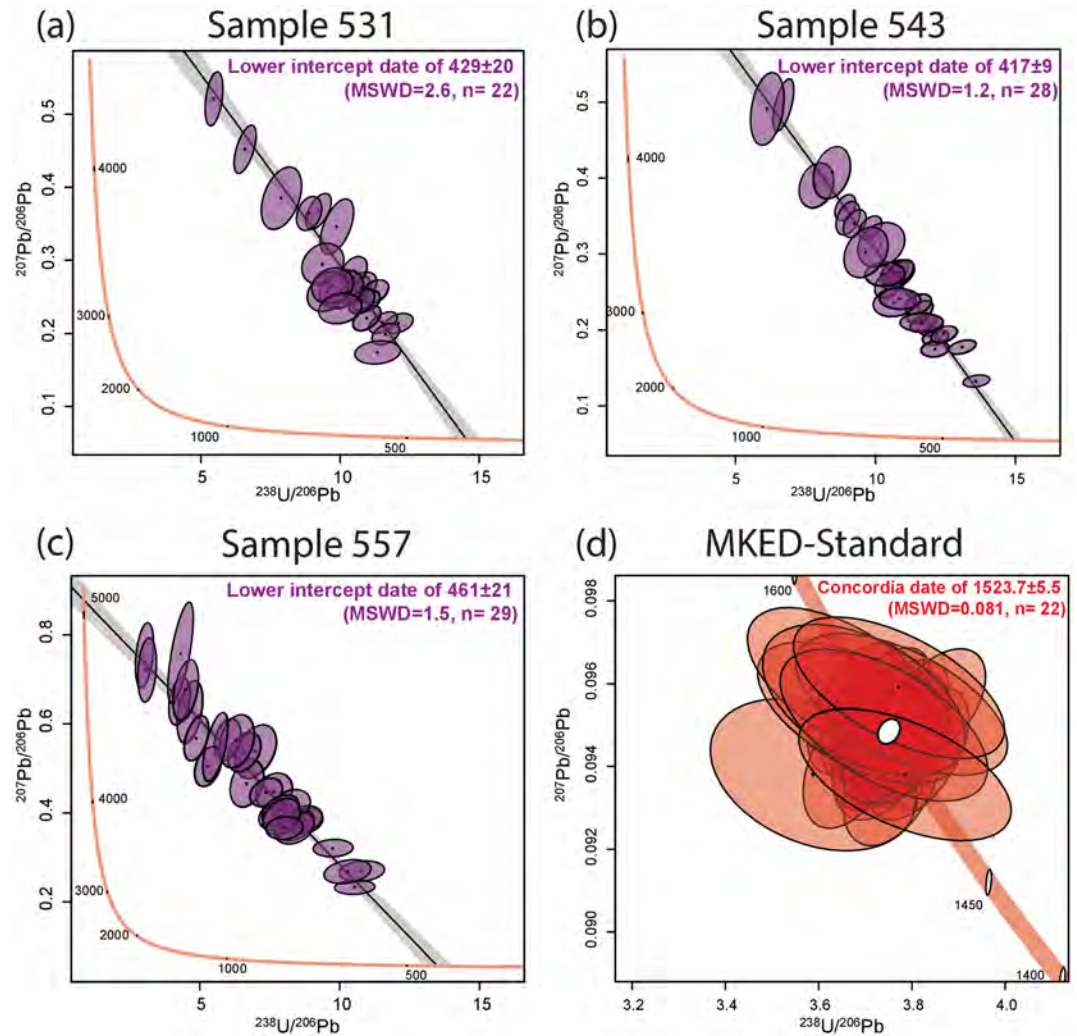


**Figure 17.** Results of in situ LA-ICP-MS U-Pb age dating of synkinematic titanite grains in the amphibolites. The results are plotted on Terra Wasserburg concordia diagrams with lower intercept dates.

Sample 640 is consistent with rhomb  $\langle a \rangle$  as the dominant active slip system during dextral shear (Figure 14e; Heilbronner & Tullis, 2006; Schmid & Casey, 1986). In summary, microstructures in both samples indicate that quartz deformed by dislocation creep accompanied by dynamic recrystallization.

In Sample 695, we interpret the quartz aggregates in the different subsets (Figure 15d) as the result of different stages of the microstructural evolution. The  $c$ -axis CPO of subset 1 is consistent with dominant prism  $\langle a \rangle$  and rhomb  $\langle a \rangle$  slip (Figure 16a). The  $c$ -axis CPO of Subset 2 is dominated by a single girdle synthetically inclined with the dextral sense of shear of the sample, and consistent with the activity of rhomb  $\langle a \rangle$ , basal  $\langle a \rangle$ , and prism  $\langle a \rangle$  slip (Figure 16b). The synthetic single girdle is weakened in Subset 3, which, although it has been sampled in a dominantly monomineralic aggregate, shows an incipient stage of phase mixing, with the local occurrence of second phases at the quartz-quartz grain boundaries. We note that large grains of Subset 3 contain subgrains of similar size to the surrounding recrystallized grains (arrows in Figure 15d). Thus, the high frequency of low angle misorientations in the misorientation angle distribution for Subset 3, together with the clustering of misorientation axes around  $\langle c \rangle$ , indicates that the main deformation mechanism in largely monomineralic Subset 3 was still dislocation creep and that dynamic recrystallization predominantly occurred by progressive subgrain rotation. The number of recrystallized grains in the subsets of Sample 695 is too low to estimate differential stresses with paleopiezometers (e.g., Cross et al., 2017; Stipp & Tullis, 2003). Our preferred interpretation, based also on the qualitative observation of subgrain size in the different subsets, is that the decrease in recrystallized grain size from Subsets 1 to 3



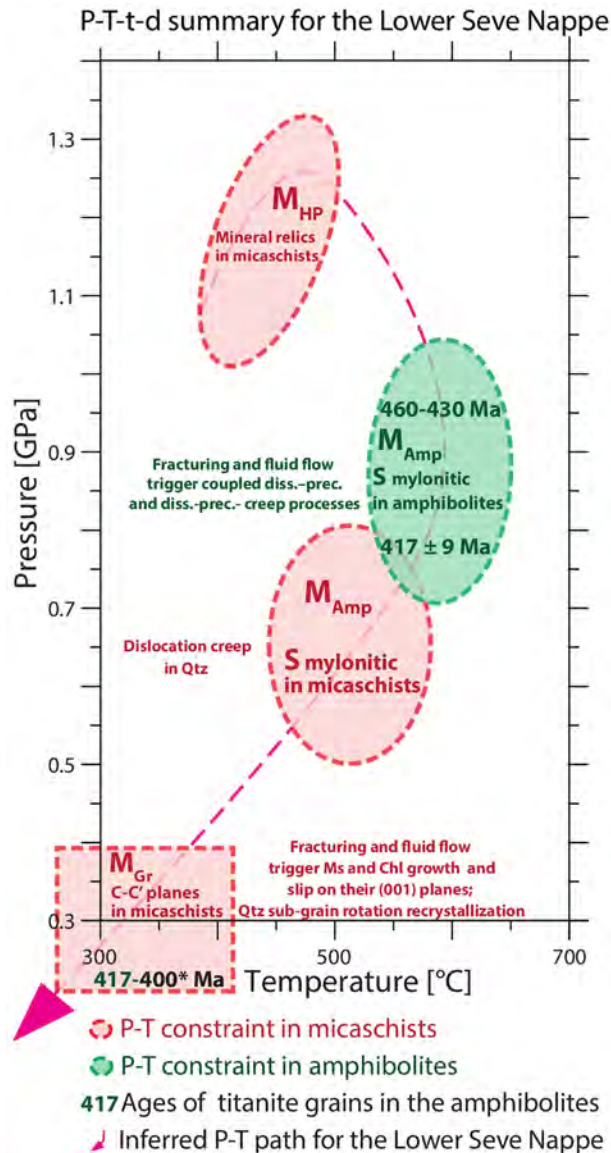


**Figure 18.** P-T-t-d summary path of the studied samples with highlighted the three metamorphic stages described in the text and the deformation mechanisms. The star indicates the youngest age constraint for the C- and C'-type shear bands from Andersen (1998) and Fossen (2000; see text for further details).

biotite into chlorite in proximity of the C and C' planes (Figure 10g). However, biotite is still preserved along most of the main mylonitic foliation (Figure 10h), thus suggesting that retrogression is mostly localized. This observation further confirms that the main infiltration of fluid occurred along the C and C' planes (e.g., Bukovská et al., 2016; Leclère et al., 2016; Wassmann & Stöckhert, 2013).

The presence of these discrete muscovite- and chlorite-rich planes promoted connectivity between weak phyllosilicate grains that strongly localized deformation and weakened the rock (Bukovská et al., 2016; Ceccato et al., 2018; Hunter et al., 2016; Mariani et al., 2006; Menegon et al., 2008; Shea & Kronenberg, 1993; Wintsch et al., 1995). Finally, the presence of such phyllosilicate-rich planes can accommodate large amount of strain, through the new mechanism of ripplocation motion (i.e., the motion of a new type of crystal defect—ripplocation—that involves a ripple of the basal layer and a basal dislocation, where the ripple enables c-axis parallel deformation in phyllosilicates; Kushima et al., 2015) rather than dislocation glide, as recently suggested by Aslin et al. (2019).

results from a progressive increase of differential stress and strain rate during strain localization under decreasing T (e.g., Hirth & Tullis, 1992; Stipp et al., 2002). However, a larger EBSD data set would be necessary to properly validate this interpretation.

Subset 4 does not show an obvious CPO, and various processes could have concurred in the development of its microstructure. The lack of CPO, coupled with the fine grain size and phase mixing, could result from dominant grain size sensitive creep deformation in polyphase C-type bands (Figures 16c and 16d). A similar evolution of quartz c-axis CPO during progressive dismembering of monomineralic aggregates and transition to dominant grain size sensitive creep deformation in polyphase mixtures was described in Kilian et al. (2011), Viegas et al. (2016), and in Gilgannon et al. (2017). However, we note that Subsets 3 and 4 are located along C planes and some of the quartz grains are truncated and pinned against chlorite and muscovite grains (Figures 15b–15d; e.g., Song & Ree, 2007). Moreover, both plagioclase core and rims are cut by the C planes, as described in section 4.1 (Figure 4g). This suggests that the C planes formed brittlely after the progressive increase of strain rate recorded by the microstructure of quartz and are the latest microstructure recorded by the rock. Thus, microfracturing of quartz grains could also occur during the formation of the C planes and contribute to grain size reduction and phase mixing observed in Subset 4. Successively, these quartz grains could have experience healing by strain-induced grain boundary migration (e.g., Lagoeiro & Barbosa, 2010; Trepmann et al., 2007).

In both micaschist samples, muscovite and chlorite grains display undulose extinction, bending, and strong CPO compatible with slip on the (001) plane (Figure S1). The presence of chlorite and muscovite crystallizing as neoblasts along C and C' planes, the dragging of the surrounding bigger muscovite grains into these planes forming mica fish, and the quartz grain size decrease by subgrain rotation recrystallization near to these planes suggest that the C planes evolved into ductile planes after a first initial brittle stage. Furthermore, these data imply that fluid influx occurred after fracturing preferentially along these brittle planes and their immediate damage zone, allowing the crystallization of chlorite and muscovite as neoblasts, since at 300–350°C solid-state diffusion is too slow and inefficient to account for the formation of those minerals (e.g., Ferry, 1994; Putnis & Putnis, 2007; Figure 18). Similarly, the main mylonitic foliation, which developed under epidote amphibolite facies conditions, was locally overprinted at lower pressure, as, for example, highlighted by the presence of chlorite in the asymmetric pressure shadows around garnet (Figure 4d) and by the progressive retrogression of

### 5.3. Evolution of the Lower Seve Nappe and Implications for the Scandinavian Caledonides

As presented in section 2, mylonitic fabrics are dominant from 1,700 m to the end of the core at 2,500 m depths. Additionally, the lowermost portion of the core is composed of strongly deformed metasediments, interpreted as representing the basal shear zone juxtaposing the Lower Seve Nappe with the Särvi Nappe (Giuntoli, Menegon, & Warren, 2018; Hedin et al., 2016; Lorenz et al., 2015). The data presented in this study quantify the metamorphic conditions and characterize the deformation mechanisms of the Lower Seve Nappe and represent the first P-T-t-d path for this unit (Figure 18). Our data suggest that the Lower Seve Nappe attained peak metamorphic conditions of 400–500°C and 1–1.3 GPa ( $M_{HP}$  in Figure 18). No fabrics are preserved for this metamorphic stage.

The older titanite dates found in this study (460–430 Ma; Figure 18) could be related to titanite growth during decompression from the peak metamorphic conditions to the incipient stages of development of the mylonitic foliation at amphibolite facies conditions (600–650°C and 0.8–1 GPa;  $M_{amp}$  in amphibolites). A similar age range of 470–445 Ma was found to reflect the eclogite facies metamorphism in the Middle Seve Nappe and other portions of the Lower Seve Nappe (Brueckner & Van Roermund, 2007; Fassmer et al., 2017; Petrik et al., 2019; Root & Corfu, 2012). In the Middle Seve successive exhumation, decompression melting and granulite facies metamorphism were constrained at 440–445 Ma and crystallization of felsic segregation and pegmatites, crosscutting the previous HT fabrics, occurred at ~435–428 Ma (Grimmer et al., 2015; Klonowska et al., 2017; Ladenberger et al., 2013; Majka et al., 2012). The tectonic contact between the Middle and Lower Seve Nappes was considered active between 434 and 426 Ma in several studies (Bender et al., 2019; Dallmeyer, 1990; Dallmeyer et al., 1985; Grimmer et al., 2015; Hacker & Gans, 2005). U-Pb titanite TIMS data from a metapsammite of the Lower Seve Nappe directly beneath the tectonic contact suggested crystallization between 437 and 427 Ma (Gromet et al., 1996). Moreover, a date of  $426.0 \pm 6.0$  Ma was obtained by in situ U-Th-Pb on monazite from a sheared migmatite at the base of the Middle Seve Nappe (Åreskutan basal shear zone; Majka et al., 2012). No P-T estimates are available for this fabric, but the minerals stable (and possibly growing) during this intense deformation period include garnet, biotite, sillimanite (fibrolite), kyanite, muscovite, and plagioclase (Arnbom, 1980) and suggest upper amphibolite facies conditions (e.g., Spear et al., 1999). Thus, the mylonitic foliation developed at the base of the Middle Seve Nappe records a similar P-T-t evolution to that proposed in this study for the Lower Seve Nappe, but at slightly higher temperature. It is worth noting that no evidence was found for metamorphism at UHP eclogite or granulite facies conditions in the Lower Seve Nappe in central Jämtland, supporting the idea that this nappe was juxtaposed with the Middle Seve Nappe as the latter was exhumed.

Successively, the Lower Seve Nappe experienced further decompression to 0.8–0.5 GPa and 600–500°C at  $417 \pm 9$  Ma (data from this study;  $M_{amp}$  in amphibolites and micaschists), the expression of which is the mylonitic foliation of epidote amphibolite facies conditions throughout middle and lower portion of the drill core (>1,000 m of thickness). Similar conditions of 480–600°C and 1–1.1 GPa were described for the Lower Seve Nappe westward from the study area (Bergman, 1992). Regionally, this foliation is associated with a stretching lineation with an E-W trend and a top-to-the-east sense of shear (Bender et al., 2018). Northward from the study area, this foliation was dated to  $432 \pm 8$  Ma by Rb-Sr multimineral isochron techniques (Gäddede area; Bender et al., 2019). This date corresponds, within uncertainty, with our study, although we cannot exclude that these dates captured two successive stages of the mylonitic foliation development or that minor age differences exist between different areas of the Lower Seve Nappe.

The retrograde evolution continued with the development of brittle to ductile C and C' planes of greenschist facies between 400°C and 300°C and ~0.3 GPa ( $M_{gr}$  in Figure 18). This fabric is visible in the lower part of the drill core (~500 m of thickness) and is more pervasive toward the bottom. It is believed to represent the thrust responsible for the juxtaposition of the Lower Seve Nappe above the Särvi Nappe (Hedin et al., 2016; Lorenz et al., 2015). These fabrics are also described from surrounding areas and correspond to the greenschist facies mylonitic zone that divides the Lower Seve Nappe from the lower Särvi Nappe (Arnbom, 1980), with a top-to-the-E-SE sense of shear (Bender et al., 2018). In particular, the latter authors did not observe any opposite sense of shear for both fabrics. Therefore, we suggest that the asymmetric fabrics recorded by our samples are compatible with a top-to-the-E-SE sense of shear.

No age data are available for the younger fabric, but it could be coeval with cooling of the Seve Nappe Complex below 350°C at ~415 Ma (Hacker & Gans, 2005) and with the younger date of  $414 \pm 4$  Ma

related to the development of the greenschist facies foliation in several nappes of the central Scandinavian Caledonides (Middle Köli Nappe, Upper Seve Nappe, and Lower Allochthon; Figure 7 of Bender et al., 2019). The youngest age constraint is provided by the date of ~400 Ma, marking the onset of normal faulting cross-cutting the tectonic contacts between the prestructured Nappes ( $^{40}\text{Ar}/^{39}\text{Ar}$  cooling ages on white mica; Andersen, 1998; Fossen, 2000).

In summary, we suggest that the fabrics described in this paper formed due to protracted and long-lasting shearing from epidote amphibolite to greenschist facies conditions during exhumation and stacking of the Lower Seve Nappe with the Middle Seve Nappe (above) and the Särvi Nappe (below). We agree with previous interpretations that the emplacement and juxtapositions of the different tectonometamorphic units occurred by a series of in- and out-of-sequence thrusts, together with syn-thrusting exhumation, starting at granulite facies conditions in the Middle Seve Nappe and at amphibolite and greenschist facies conditions in all the other nappes (Bender et al. (2018, 2019). Moreover, this study highlights that (1) late (presumably out-of-sequence) Caledonian thrusting appears to be facilitated by fracturing and fluid infiltration along discrete, localized shear bands, and (2) exhumation of the Lower Seve Nappe from ~1 to ~0.3 GPa was coeval with crustal shortening, similar to what observed in the hinterland of other mountain belts (e.g., Le Bayon & Balleuvre, 2006).

## 6. Conclusions

A multianalysis approach including petrographic and microstructural analyses, thermodynamic modeling, EBSD analyses, and age dating has allowed the reconstruction of the first pressure-temperature-time-deformation path for the COSC-1 drill core (Lower Seve Nappe) in the Scandinavian Caledonides. The data suggest that the ~1 km-thick main mylonitic foliation formed at epidote amphibolite facies conditions during the retrograde path from 600°C, 1 GPa to 500°C, 0.5 GPa at around 417 ± 9 Ma. The older ages found in the amphibolites (460–430 Ma) may be related to incipient stages of development of the mylonitic amphibolite facies foliation. Mineral relics in micaschists highlight an older high-pressure stage between 400–500°C and 1–1.3 GPa.

Toward the bottom of the drill core the mylonitic foliation is overprinted by a discrete, brittle-to-ductile C and C' shear bands, developed at lower metamorphic conditions of 300–400°C and ~0.3 GPa. An initial brittle failure allowed preferential fluid influx along these planes and facilitated the neo-crystallization of chlorite and white mica. Strain localized proximal to those planes, as reflected by grain size reduction due to subgrain rotation recrystallization in the quartz rich layers. Incipient to progressive dismembering of monomineralic aggregates occurred, with transition to dominant grain size sensitive creep deformation in poly-phase mixtures that further weakened the rock. We interpret this fabric as the expression of the thrust at the base of the Seve Nappe Complex, responsible for the exhumation and juxtaposition of this nappe with the lower Särvi Nappe. The age range for this younger fabric is comprised between 417 (the youngest age of the main mylonitic foliation) and 400 Ma, the latter age marking the onset of normal faulting in the Scandinavian Caledonides.

The results suggest that these fabrics formed due to protracted and long-lasting shearing from epidote amphibolite to greenschist facies conditions and facilitated the exhumation and juxtaposition of the Seve Nappe Complex against the Särvi Nappe in the Caledonian nappe stack.

## Data Availability Statement

The data presented in the manuscript are available in the main text, tables, figures, supporting information, the references, and in the Mendeley Data repository (<https://doi.org/10.17632/2v6rj69mzv.2>).

## References

- Andersen, T. B. (1998). Extensional tectonics in the Caledonides of southern Norway, an overview. *Tectonophysics*, 285(3), 333–351.
- Anderson, J. L., & Smith, D. R. (1995). The effects of temperature and  $f\text{O}_2$  on the Al-in-hornblende barometer. *American Mineralogist*, 80(5–6), 549–559.
- Anderson, M. W., Barker, A. J., Bennett, D. G., & Dallmeyer, R. D. (1992). A tectonic model for Scandian terrane accretion in the northern Scandinavian Caledonides. *Journal of the Geological Society*, 149(5), 727–741.
- Andréasson, P. G. (1994). The Baltoscandian margin in Neoproterozoic-early Palaeozoic times. Some constraints on terrane derivation and accretion in the Arctic Scandinavian Caledonides. *Tectonophysics*, 231, (1–3), 1–32.

## Acknowledgments

A. Ceccato, I. Klonowska, and J. Majka are acknowledged for fruitful discussions. S. Hammond and D. Johnson are warmly thanked for the help with EPMA and SEM analyses, respectively. The staff at Plymouth University Electron Microscopy Centre is acknowledged for the support during EBSD analysis. Lucy Campbell is thanked for her help with Channel 5. B. Almqvist and N. Roberts are acknowledged for their support in acquiring the samples. This work was funded by an Early Postdoc. Mobility grant (project number: P2BEP2\_168722) by the Swiss National Science Foundation to F. G. and by a FP7 Marie Curie Career Integration Grant to L. M. (Grant Agreement PCIG13-GA-2013-618289). The COSC-1 drilling operations were supported by the International Continental Scientific Drilling Program (ICDP) and the Swedish Research Council (Vetenskapsrådet), and the Swedish national research infrastructure for scientific drilling “Riksriggen.” We thank Elisabetta Mariani, Zoe Braden, Richard D. Law, and Calvin Mako for their very thorough reviews and Laurent Jolivet for editorial handling.

- Arnbom, J.-O. (1980). Metamorphism of the Seve Nappes at Åreskutan, Swedish Caledonides. *Geologiska Föreningen i Stockholm Förhandlingar*, 102, 359–371. <https://doi.org/10.1080/1103589009454493>
- Aslin, J., Mariani, E., Dawson, K., & Barsoum, M. W. (2019). Ripplifications provide a new mechanism for the deformation of phyllosilicates in the lithosphere. *Nature Communications*, 10(1), 686. <https://doi.org/10.1038/s41467-019-08587-2>
- Austrheim, H. (1987). Eclogitization of lower crustal granulites by fluid migration through shear zones. *Earth and Planetary Science Letters*, 81, 221–232. [https://doi.org/10.1016/0012-821X\(87\)90158-0](https://doi.org/10.1016/0012-821X(87)90158-0)
- Bender, H., Glodny, J., & Ring, U. (2019). Absolute timing of Caledonian orogenic wedge assembly, Central Sweden, constrained by Rb-Sr multi-mineral isochron data. *Lithos*, 344–345, 339–359. <https://doi.org/10.1016/j.lithos.2019.06.033>
- Bender, H., Ring, U., Almqvist, B. S. G., Grasemann, B., & Stephens, M. B. (2018). Metamorphic zonation by out-of-sequence thrusting at back-stepping subduction zones: Sequential accretion of the Caledonian internides, central Sweden. *Tectonics*, 37, 3545–3576. <https://doi.org/10.1029/2018TC005088>
- Bergman, S. (1992). P-T paths in the Handöl area, central Scandinavia: Record of Caledonian accretion of outboard rocks to the Baltoscandian margin. *Journal of Metamorphic Geology*, 10(2), 265–281. <https://doi.org/10.1111/j.1525-1314.1992.tb00082.x>
- Bergman, S., & Sjöström, H. (1997). Accretion and lateral extension in an orogenic wedge: Evidence from a segment of the Seve-Ko'li terrane boundary, central Scandinavian Caledonides. *Journal of Structural Geology*, 19(8), 1073–1091. [https://doi.org/10.1016/S0191-8141\(97\)00028-X](https://doi.org/10.1016/S0191-8141(97)00028-X)
- Berman, R. G. (1988). Internally consistent thermodynamic data for minerals in the system Na<sub>2</sub>O-K<sub>2</sub>O-CaO-MgO-FeO-Fe<sub>2</sub>O<sub>3</sub>-Al<sub>2</sub>O<sub>3</sub>-SiO<sub>2</sub>-TiO<sub>2</sub>-H<sub>2</sub>O-CO<sub>2</sub>. *Journal of Petrology*, 29(2), 445–522.
- Berman, R. G. (1990). Mixing properties of Ca-Mg-Fe-Mn garnets. *American Mineralogist*, 75, 328–344.
- Bhadra, S., & Bhattacharya, A. (2007). The barometer tremolite + tschermakite + 2 albite = 2 pargasite + 8 quartz: Constraints from experimental data at unit silica activity, with application to garnet-free natural assemblages. *American Mineralogist*, 92(4), 491–502.
- Brander, L., Svahnberg, H., & Piazzolo, S. (2012). Brittle-plastic deformation in initially dry rocks at fluid-present conditions: transient behaviour of feldspar at mid-crustal levels. *Contributions to Mineralogy and Petrology*, 163(3), 403–425.
- Bruceknier, H. K., & van Roermund, H. L. M. (2004). Dunk tectonics: A multiple subduction/duction model for the evolution of the Scandinavian Caledonides. *Tectonics*, 23, TC2004. <https://doi.org/10.1029/2003TC001502>
- Bruceknier, H. K., & Van Roermund, H. L. M. (2007). Concurrent HP metamorphism on both margins of Iapetus: Ordovician ages for eclogites and garnet pyroxenites from the Seve Nappe Complex, Swedish Caledonides. *Journal of the Geological Society*, 164(1), 117–128.
- Bukovská, Z., Jeřábek, P., & Morales, L. F. G. (2016). Major softening at brittle-ductile transition due to interplay between chemical and deformation processes: An insight from evolution of shear bands in the South Armorican Shear Zone. *Journal of Geophysical Research: Solid Earth*, 121, 1158–1182. <https://doi.org/10.1002/2015JB012319>
- Ceccato, A., Menegon, L., Pennacchioni, G., & Morales, L. F. G. (2018). Myrmekite and strain weakening in granitoid mylonites. *Solid Earth*, 9(6), 1399–1419. <https://doi.org/10.5194/se-9-1399-2018>
- Chew, D. M., Petrus, J. A., & Kamber, B. S. (2014). U-Pb LA-ICPMS dating using accessory mineral standards with variable common Pb. *Chemical Geology*, 363, 185–199. <https://doi.org/10.1016/j.chemgeo.2013.11.006>
- Cross, A. J., Prior, D. J., Stipp, M., & Kidder, S. (2017). The recrystallized grain size piezometer for quartz: An EBSD-based calibration. *Geophysical Research Letters*, 44, 6667–6674. <https://doi.org/10.1002/2017GL073836>
- Dallmeyer, R. D. (1990). 40Ar/39Ar mineral age record of a polyorogenic evolution within the Seve and Köli nappes, Trøndelag, Norway. *Tectonophysics*, 179(3–4), 199–226.
- Dallmeyer, R. D., Gee, D. G., & Beckholmen, M. (1985). 40 Ar/39 Ar mineral age record of early Caledonian tectonothermal activity in the Baltoscandian Miogeocline, central Scandinavia. *American Journal of Science*, 285(6), 532–568.
- De Capitani, C., & Brown, T. H. (1987). The computation of chemical equilibrium in complex systems containing non-ideal solutions. *Geochimica et Cosmochimica Acta*, 51, 2639–2652.
- de Capitani, C., & Petrakakis, K. (2010). The computation of equilibrium assemblage diagrams with Theriak/Domino software. *American Mineralogist*, 95(7), 1006–1016. <https://doi.org/10.2138/am.2010.3354>
- Dempsey, E. D., Prior, D. J., Mariani, E., Toy, V. G., & Tatham, D. J. (2011). Mica-controlled anisotropy within mid-to-upper crustal mylonites: An EBSD study of mica fabrics in the Alpine Fault Zone, New Zealand. *Geological Society, London, Special Publications*, 360(1), 33–47.
- Dubacq, B., Vidal, O., & De Andrade, V. (2010). Dehydration of dioctahedral aluminous phyllosilicates: Thermodynamic modelling and implications for thermobarometric estimates. *Contributions to Mineralogy and Petrology*, 159(2), 159.
- Faber, C., Stünitz, H., Gasser, D., Jeřábek, P., Kraus, K., Corfu, F., et al. (2019). Anticlockwise metamorphic pressure-temperature paths and nappe stacking in the Reisa Nappe Complex in the Scandinavian Caledonides, northern Norway: Evidence for weakening of lower continental crust before and during continental collision. *Solid Earth*, 10(1), 117–148. <https://doi.org/10.5194/se-10-117-2019>
- Fassmer, K., Klonowska, I., Walczak, K., Andersson, B., Froitzeim, N., Majka, J., et al. (2017). Middle Ordovician subduction of continental crust in the Scandinavian Caledonides: an example from Tjeliken, Seve Nappe Complex, Sweden. *Contributions to Mineralogy and Petrology*, 172(11–12), 103. <https://doi.org/10.1007/s00410-017-1420-7>
- Ferry, J. M. (1994). A historical review of metamorphic fluid flow. *Journal of Geophysical Research*, 99(B8), 15,415–15,498.
- Fossen, H. (2000). Extensional tectonics in the Caledonides: Synorogenic or postorogenic? *Tectonics*, 19(2), 213–224.
- Fossen, H., & Rykkelid, E. (1992). Postcollisional extension of the Caledonide orogen in Scandinavia: Structural expressions and tectonic significance. *Geology*, 20(8), 737–740.
- Fuhrman, M. L., & Lindsley, D. H. (1988). Ternary-feldspar modeling and thermometry. *American Mineralogist*, 73, 201–216.
- Fussey, F., Handy, M. R., & Schrank, C. (2006). Networking of shear zones at the brittle-to-viscous transition (Cap de Creus, NE Spain). *Journal of Structural Geology*, 28(7), 1228–1243.
- Gasser, D., Jeřábek, P., Faber, C., Stünitz, H., Menegon, L., Corfu, F., et al. (2015). Behaviour of geochronometers and timing of metamorphic reactions during deformation at lower crustal conditions: Phase equilibrium modelling and U-Pb dating of zircon, monazite, rutile and titanite from the Kalak Nappe Complex, northern Norway. *Journal of Metamorphic Geology*, 33(5), 513–534. <https://doi.org/10.1111/jmg.12131>
- Gayer, R. A., Rice, A. H. N., Roberts, D., Townsend, C., & Welbon, A. (1987). Restoration of the Caledonian Baltoscandian margin from balanced cross-sections: the problem of excess continental crust. *Transactions of the Royal Society of Edinburgh: Earth Sciences*, 78(03), 197–217.
- Gee, D. G. (1975). A tectonic model for the central part of the Scandinavian Caledonides. *American Journal of Science*, 275(A), 468–515.
- Gee, D. G., Fossen, H., Henriksen, N., & Higgins, A. K. (2008). From the early Paleozoic platforms of Baltica and Laurentia to the Caledonide Orogen of Scandinavia and Greenland. *Episodes*, 31(1), 44–51.

- Gee, D. G., Janák, M., Majka, J., Robinson, P., & van Roermund, H. (2013). Subduction along and within the Baltoscandian margin during closing of the Iapetus Ocean and Baltica-Laurentia collision. *Lithosphere*, *5*(2), 169–178.
- Gee, D. G., Juhlin, C., Pascal, C., & Robinson, P. (2010). Collisional orogeny in the Scandinavian Caledonides (COSC). *GFF*, *132*(1), 29–44.
- Gerald, J. D. F., & Stünitz, H. (1993). Deformation of granulites at low metamorphic grade. I: Reactions and grain size reduction. *Tectonophysics*, *221*(3), 269–297.
- Gilgannon, J., Füsseis, F., Menegon, L., Regenauer-Lieb, K., & Buckman, J. (2017). Hierarchical creep cavity formation in an ultramylonite and implications for phase mixing. *Solid Earth*, *8*(6), 1193–1209. <https://doi.org/10.5194/se-8-1193-2017>
- Gilio, M., Clos, F., & van Roermund, H. L. M. (2015). The Friningen Garnet Peridotite (central Swedish Caledonides). A good example of the characteristic PTt path of a cold mantle wedge garnet peridotite. *Lithos*, *230*, 1–16.
- Gilotti, J. A. (1989). Reaction progress during mylonitization of basaltic dikes along the Särvi thrust, Swedish Caledonides. *Contributions to Mineralogy and Petrology*, *101*(1), 30–45.
- Giuntoli, F., & Engi, M. (2016). Internal geometry of the central Sesia Zone (Aosta Valley, Italy): HP tectonic assembly of continental slices. *Swiss Journal of Geosciences*, *109*(3), 445–471.
- Giuntoli, F., Lanari, P., Burn, M., Eva Kunz, B., & Engi, M. (2018). Deeply subducted continental fragments—Part 2: Insight from petrochronology in the central Sesia Zone (western Italian Alps). *Solid Earth*, *9*(1). <https://doi.org/10.5194/se-9-191-2018>
- Giuntoli, F., Menegon, L., & Warren, C. J. (2018). Replacement reactions and deformation by dissolution and precipitation processes in amphibolites. *Journal of Metamorphic Geology*, *36*(9), 1263–1286. <https://doi.org/10.1111/jmg.12445>
- Giuntoli, F., Vitale Brovarone, A., & Menegon, L. (2020). Feedback between high-pressure genesis of abiotic methane and strain localization in subducted carbonate rocks. *Scientific Reports*, *10*(1), 9848. <https://doi.org/10.1038/s41598-020-66640-3>
- Grimmer, J. C., Glodny, J., Drüppel, K., Greiling, R. O., & Kontny, A. (2015). Early-to mid-Silurian extrusion wedge tectonics in the central Scandinavian Caledonides. *Geology*, *43*(4), 347–350.
- Gromet, L. P., Sjöström, H., Bergman, S., Claesson, S., Essex, R. M., Andréasson, P. G., & Albrecht, L. (1996). Contrasting ages of metamorphism in the Seve nappes: U-Pb results from the central and northern Swedish Caledonides. *GFF*, *118*(sup004), 36–37. <https://doi.org/10.1080/11035899609546308>
- Hacker, B. R., & Gans, P. B. (2005). Continental collisions and the creation of ultrahigh-pressure terranes: Petrology and thermochronology of nappes in the central Scandinavian Caledonides. *Geological Society of America Bulletin*, *117*(1–2), 117–134.
- Hartnady, M. I. H., Kirkland, C. L., Clark, C., Spaggiari, C. V., Smithies, R. H., Evans, N. J., & McDonald, B. J. (2019). Titanite dates crystallisation; slow Pb diffusion during super-solidus re-equilibration. *Journal of Metamorphic Geology*, *37*, 823–838. <https://doi.org/10.1111/jmg.12489>
- Heaman, L. M. (2009). The application of U-Pb geochronology to mafic, ultramafic and alkaline rocks: An evaluation of three mineral standards. *Chemical Geology*, *261*(1), 43–52. <https://doi.org/10.1016/j.chemgeo.2008.10.021>
- Hedin, P., Almqvist, B., Berthet, T., Juhlin, C., Buske, S., Simon, H., et al. (2016). 3D reflection seismic imaging at the 2.5 km deep COSC-1 scientific borehole, central Scandinavian Caledonides. *Tectonophysics*, *689*, 40–55. <https://doi.org/10.1016/j.tecto.2015.12.013>
- Heilbronner, R., & Tullis, J. (2006). Evolution of c axis pole figures and grain size during dynamic recrystallization: Results from experimentally sheared quartzite. *Journal of Geophysical Research*, *111*, B10202. <https://doi.org/10.1029/2005JB004194>
- Hirth, G., & Tullis, J. A. N. (1992). Dislocation creep regimes in quartz aggregates. *Journal of Structural Geology*, *14*(2), 145–159.
- Holland, T., & Blundy, J. (1994). Non-ideal interactions in calcic amphiboles and their bearing on amphibole-plagioclase thermometry. *Contributions to Mineralogy and Petrology*, *116*(4), 433–447.
- Hunter, N. J. R., Hasalová, P., Weinberg, R. F., & Wilson, C. J. L. (2016). Fabric controls on strain accommodation in naturally deformed mylonites: The influence of interconnected micaceous layers. *Journal of Structural Geology*, *83*, 180–193.
- Hunziker, P. (2003). The stability of tri-octahedral Fe<sup>2+</sup>-Mg-Al chlorite: A combined experimental and theoretical study. Mineralogisch-Petrographisches Institut der Universität.
- Janák, M., Froitzheim, N., Vrabec, M., Ravna, E. J. K., & deHoog, C.-J. (2006). Ultrahigh-pressure metamorphism and exhumation of garnet peridotite in Pohorje, Eastern Alps. *Journal of Metamorphic Geology*, *24*, 19–31.
- Janák, M., van Roermund, H., Majka, J., & Gee, D. (2013). UHP metamorphism recorded by kyanite-bearing eclogite in the Seve Nappe Complex of northern Jämtland, Swedish Caledonides. *Gondwana Research*, *23*(3), 865–879.
- Jolivet, L., Faccenna, C., Goffé, B., Mattei, M., Rossetti, F., Brunet, C., et al. (1998). Midcrustal shear zones in postorogenic extension: Example from the northern Tyrrhenian Sea. *Journal of Geophysical Research*, *103*(B6), 12,123–12,160. <https://doi.org/10.1029/97JB03616>
- Keller, L. M., De Capitani, C., & Abart, R. (2005). A quaternary solution model for white micas based on natural coexisting phengite-paragonite pairs. *Journal of Petrology*, *46*(10), 2129–2144. <https://doi.org/10.1093/petrology/egi050>
- Kilian, R., Heilbronner, R., & Stünitz, H. (2011). Quartz grain size reduction in a granulite rock and the transition from dislocation to diffusion creep. *Journal of Structural Geology*, *33*(8), 1265–1284. <https://doi.org/10.1016/j.jsg.2011.05.004>
- Kjøll, H. J., Viola, G., Menegon, L., & Sørensen, B. E. (2015). Brittle-viscous deformation of vein quartz under fluid-rich lower greenschist facies conditions. *Solid Earth*, *6*(2), 681.
- Klonowska, I., Janák, M., Majka, J., Froitzheim, N., & Košmińska, K. (2016). Eclogite and garnet pyroxenite from Stor Jougdan, Seve Nappe Complex, Sweden: implications for UHP metamorphism of allochthons in the Scandinavian Caledonides. *Journal of Metamorphic Geology*, *34*(2), 103–119.
- Klonowska, I., Janák, M., Majka, J., Petrik, I., Froitzheim, N., Gee, D. G., & Sasinková, V. (2017). Microdiamond on Åreskutan confirms regional UHP metamorphism in the Seve Nappe Complex of the Scandinavian Caledonides. *Journal of Metamorphic Geology*, *35*(5), 541–564. <https://doi.org/10.1111/jmg.12244>
- Kohn, M. J. (2017). Titanite petrochronology. *Reviews in Mineralogy and Geochemistry*, *83*(1), 419–441.
- Kushima, A., Qian, X., Zhao, P., Zhang, S., & Li, J. (2015). Ripplifications in van der Waals layers. *Nano Letters*, *15*(2), 1302–1308.
- Ladenberger, A., Be'eri-Shlevin, Y., Claesson, S., Gee, D. G., Majka, J., & Romanova, I. V. (2013). Tectonometamorphic evolution of the Åreskutan Nappe-Caledonian history revealed by SIMS U-Pb zircon geochronology. Geological Society, London, Special Publications, 390, SP390. 10.
- Lagoeiro, L., & Barbosa, P. (2010). Nucleation and growth of new grains in recrystallized quartz vein: An example from banded iron formation in Iron Quadrangle, Brazil. *Journal of Structural Geology*, *32*(4), 595–604. <https://doi.org/10.1016/j.jsg.2010.03.007>
- Lanari, P. (2012). Micro-cartographie P-T-e dans les roches métamorphiques. Applications aux Alpes et à l'Himalaya. Université de Grenoble. Grenoble.
- Lanari, P., & Engi, M. (2017). Local bulk composition effects on metamorphic mineral assemblages. *Reviews in Mineralogy and Geochemistry*, *83*, 55–102. <https://doi.org/10.2138/rmg.2017.83.1>

- Lanari, P., Giuntoli, F., Loury, C., Burn, M., & Engi, M. (2017). An inverse modeling approach to obtain P-T conditions of metamorphic stages involving garnet growth and resorption. *European Journal of Mineralogy*, *29*(2), 181–199. <https://doi.org/10.1127/ejm/2017/0029-2597>
- Lanari, P., Guillot, S., Schwartz, S., Vidal, O., Tricart, P., Riel, N., & Beyssac, O. (2012). Diachronous evolution of the alpine continental subduction wedge: Evidence from P-T estimates in the Briançonnais Zone houillere (France-Western Alps). *Journal of Geodynamics*, *56–57*, 39–54.
- Lanari, P., Vidal, O., Lewin, E., Dubacq, B., Andrade, V., & Schwartz, S. (2014). XMapTools a Matlab®-based graphic user interface for microprobe quantified image processing. *Computers and Geosciences*, *62*, 227–240. <https://doi.org/10.1016/j.cageo.2013.08.010>
- Le Bayon, B., & Balleve, M. (2006). Deformation history of a subducted continental crust (Gran Paradiso, Western Alps): Continuing crustal shortening during exhumation. *Journal of Structural Geology*, *28*(5), 793–815.
- Leclère, H., Faulkner, D., Wheeler, J., & Mariani, E. (2016). Permeability control on transient slip weakening during gypsum dehydration: Implications for earthquakes in subduction zones. *Earth and Planetary Science Letters*, *442*, 1–12.
- Lloyd, G. E. (2004). Microstructural evolution in a mylonitic quartz simple shear zone: the significant roles of dauphine twinning and misorientation. *Geological Society, London, Special Publications*, *224*(1), 39–61.
- Lorenz, H., Rosberg, J. E., Juhlin, C., Bjelm, L., Almqvist, B. S. G., Berthet, T., et al. (2015). COSC-1-drilling of a subduction-related allochthon in the Palaeozoic Caledonide orogen of Scandinavia. *Scientific Drilling*, *19*, 1–11. <https://doi.org/10.5194/sd-19-1-2015>
- Mäder, U. K., & Berman, R. G. (1992). *Amphibole thermobarometry: a thermodynamic approach*. Ottawa: Geological Survey of Canada.
- Mäder, U. K., Percival, J. A., & Berman, R. G. (1994). Thermobarometry of garnet-clinopyroxene-hornblende granulites from the Kapuskasing structural zone. *Canadian Journal of Earth Sciences*, *31*(7), 1134–1145.
- Majka, J., Be'eri-Shlevin, Y., Gee, D. G., Ladenberger, A., Claesson, S., Konecny, P., & Klonowska, I. (2012). Multiple monazite growth in the Åreskutan migmatite: evidence for a polymetamorphic Late Ordovician to Late Silurian evolution in the Seve Nappe Complex of west-central Jamtland, Sweden. *Journal of Geosciences*, *57*(1), 3–23.
- Majka, J., Rosén, Å., Janák, M., Froitzheim, N., Klonowska, I., Manecki, M., et al. (2014). Microdiamond discovered in the Seve Nappe (Scandinavian Caledonides) and its exhumation by the “vacuum-cleaner” mechanism. *Geology*, *42*(12), 1107–1110. <https://doi.org/10.1130/G36108.1>
- Mancktelow, N. S., & Pennacchioni, G. (2005). The control of precursor brittle fracture and fluid-rock interaction on the development of single and paired ductile shear zones. *Journal of Structural Geology*, *27*(4), 645–661.
- Mariani, E., Brodie, K. H., & Rutter, E. H. (2006). Experimental deformation of muscovite shear zones at high temperatures under hydrothermal conditions and the strength of phyllosilicate-bearing faults in nature. *Journal of Structural Geology*, *28*(9), 1569–1587.
- Menegon, L., Pennacchioni, G., Heilbronner, R., & Pittarello, L. (2008). Evolution of quartz microstructure and c-axis crystallographic preferred orientation within ductile deformed granitoids (Arolla unit, Western Alps). *Journal of Structural Geology*, *30*(11), 1332–1347.
- Menegon, L., Piazzolo, S., & Pennacchioni, G. (2011). The effect of Dauphiné twinning on plastic strain in quartz. *Contributions to Mineralogy and Petrology*, *161*(4), 635–652. <https://doi.org/10.1007/s00410-010-0554-7>
- Menegon, L., Stünitz, H., Nasipuri, P., Heilbronner, R., & Svahnberg, H. (2013). Transition from fracturing to viscous flow in granulite facies perthitic feldspar (Lofoten, Norway). *Journal of Structural Geology*, *48*, 95–112.
- Merz, L., Almqvist, B. S. G., Grimmer, J. C., & Kontny, A. (2019). Magnetic fabric development in the Lower Seve thrust from the COSC-1 drilling, Swedish Caledonides. *Tectonophysics*, *751*, 212–228. <https://doi.org/10.1016/j.tecto.2018.12.018>
- Nagel, T., de Capitani, C., & Frey, M. (2002). Isograd and P-T evolution in the eastern Lepontine Alps (Graubünden, Switzerland). *Journal of Metamorphic Geology*, *20*, 309–324.
- Neumann, B. (2000). Texture development of recrystallised quartz polycrystals unravelled by orientation and misorientation characteristics. *Journal of Structural Geology*, *22*(11–12), 1695–1711.
- Papapavlou, K., Darling, J. R., Lightfoot, P. C., Lasalle, S., Gibson, L., Storey, C. D., & Moser, D. (2018). Polyorogenic reworking of ore-controlling shear zones at the South Range of the Sudbury impact structure: A telltale story from in situ U–Pb titanite geochronology. *Terra Nova*, *30*(3), 254–261. <https://doi.org/10.1111/ter.12332>
- Papapavlou, K., Darling, J. R., Storey, C. D., Lightfoot, P. C., Moser, D. E., & Lasalle, S. (2017). Dating shear zones with plastically deformed titanite: New insights into the orogenic evolution and ore remobilization history of the Sudbury impact structure (Ontario, Canada). *Precambrian Research*, *291*, 220–235.
- Petrík, I., Janák, M., Klonowska, I., Majka, J., Froitzheim, N., Yoshida, K., et al. (2019). Monazite behaviour during metamorphic evolution of a diamond-bearing gneiss: a case study from the Seve Nappe Complex, Scandinavian Caledonides. *Journal of Petrology*, *60*(9), 1773–1796.
- Prior, D. J., Boyle, A. P., Brenker, F., Cheadle, M. C., Day, A., Lopez, G., et al. (1999). The application of electron backscatter diffraction and orientation contrast imaging in the SEM to textural problems in rocks. *American Mineralogist*, *84*(11–12), 1741–1759. <https://doi.org/10.2138/am-1999-11-1204>
- Prior, D. J., Mariani, E., & Wheeler, J. (2009). EBSD in the Earth sciences: Applications, common practice, and challenges. In *Electron backscatter diffraction in materials science* (pp. 345–360). New York: Springer.
- Prior, D. J., Wheeler, J., Peruzzo, L., Spiess, R., & Storey, C. (2002). Some garnet microstructures: An illustration of the potential of orientation maps and misorientation analysis in microstructural studies. *Journal of Structural Geology*, *24*(6), 999–1011.
- Putnis, A. (2015). Transient porosity resulting from fluid-mineral interaction and its consequences. *Reviews in Mineralogy and Geochemistry*, *80*, 1–23.
- Putnis, A., & Putnis, C. V. (2007). The mechanism of reequilibration of solids in the presence of a fluid phase. *Journal of Solid State Chemistry*, *180*(5), 1783–1786.
- Rice, A. H. N., & Anderson, M. W. (2016). Restoration of the external Scandinavian Caledonides. *Geological Magazine*, 1–30.
- Roberts, D. (2003). The Scandinavian Caledonides: Event chronology, palaeogeographic settings and likely modern analogues. *Tectonophysics*, *365*(1), 283–299.
- Roberts, D., & Gee, D. G. (1985). An introduction to the structure of the Scandinavian Caledonides. *The Caledonide Orogen–Scandinavia and Related Areas*, *1*, 55–68.
- Root, D., & Corfu, F. (2012). U–Pb geochronology of two discrete Ordovician high-pressure metamorphic events in the Seve Nappe Complex, Scandinavian Caledonides. *Contributions to Mineralogy and Petrology*, *163*(5), 769–788.
- Schmid, S. M., & Casey, M. (1986). Complete fabric analysis of some commonly observed quartz c-axis patterns. *Mineral and Rock Deformation*, 263–286.
- Searle, M. P., Law, R. D., Godin, L., Larson, K. P., Streule, M. J., Cottle, J. M., & Jessup, M. J. (2008). Defining the Himalayan main central thrust in Nepal. *Journal of the Geological Society*, *165*(2), 523–534.

- Shea, W. T., & Kronenberg, A. K. (1993). Strength and anisotropy of foliated rocks with varied mica contents. *Journal of Structural Geology*, *15*(9–10), 1097–1121.
- Sjöström, H. (1983). The Seve-Köli Nappe Complex of the Handöl-Storlien-Essandsjøen area, Scandinavian Caledonides. *Geologiska Föreningen i Stockholm Förhandlingar*, *105*(2), 93–117.
- Song, W. J., & Ree, J.-H. (2007). Effect of mica on the grain size of dynamically recrystallized quartz in a quartz-muscovite mylonite. *Journal of Structural Geology*, *29*(12), 1872–1881. <https://doi.org/10.1016/j.jsg.2007.09.011>
- Spandler, C., Hammerli, J., Sha, P., Hilbert-Wolf, H., Hu, Y., Roberts, E., & Schmitz, M. (2016). MKED1: A new titanite standard for in situ analysis of Sm-Nd isotopes and U-Pb geochronology. *Chemical Geology*, *425*, 110–126. <https://doi.org/10.1016/j.chemgeo.2016.01.002>
- Spear, F. S., Kohn, M. J., & Cheney, J. T. (1999). P-T paths from anatexis pelites. *Contributions to Mineralogy and Petrology*, *134*(1), 17–32.
- Spencer, K. J., Hacker, B. R., Kylander-Clark, A. R. C., Andersen, T. B., Cottle, J. M., Stearns, M. A., et al. (2013). Campaign-style titanite U-Pb dating by laser-ablation ICP: Implications for crustal flow, phase transformations and titanite closure. *Chemical Geology*, *341*, 84–101. <https://doi.org/10.1016/j.chemgeo.2012.11.012>
- Stephens, M. B. (1988). The Scandinavian Caledonides: A complexity of collisions. *Geology Today*, *4*(1), 20–26.
- Stipp, M., Stünitz, H., Heilbronner, R., & Schmid, S. M. (2002). Dynamic recrystallization of quartz: Correlation between natural and experimental conditions. *Geological Society, London, Special Publications*, *200*(1), 171–190.
- Stipp, M., & Tullis, J. (2003). The recrystallized grain size piezometer for quartz. *Geophysical Research Letters*, *30*(21), 2088. <https://doi.org/10.1029/2003GL018444>
- Strömberg, A., Karis, L., Zachrisson, E., Sjöstrand, T., Skoglund, R., Lundegårdh, P.H., et al. (1984). Berggrundskarta över Jämtlands län utom förutvarande Fjällsjö kommun, scale 1: 200 000. Geological Survey of Sweden, Ca. 53.
- Stünitz, H., & Gerald, J. D. F. (1993). Deformation of granitoids at low metamorphic grade. II: Granular flow in albite-rich mylonites. *Tectonophysics*, *221*(3–4), 299–324.
- Trepmann, C. A., Stöckhert, B., Dörner, D., Moghadam, R. H., Küster, M., & Röller, K. (2007). Simulating coseismic deformation of quartz in the middle crust and fabric evolution during postseismic stress relaxation—An experimental study. *Tectonophysics*, *442*(1–4), 83–104.
- Van Roermund, H. L. M. (1985). Eclogites of the Seve nappe, central Scandinavian Caledonides. *The Caledonide Orogen—Scandinavia and Related Areas*, 873–886.
- Van Roermund, H. L. M. (1989). High-pressure ultramafic rocks from the allochthonous nappes of the Swedish Caledonides. *The Caledonide Geology of Scandinavia*, 205–219.
- Vermeesch, P. (2018). IsoplotR: A free and open toolbox for geochronology. *Geoscience Frontiers*, *9*(5), 1479–1493. <https://doi.org/10.1016/j.gsf.2018.04.001>
- Vidal, O., De Andrade, V., Lewin, E., Munoz, M., Parra, T., & Pascarelli, S. (2006). P-T-deformation-Fe<sup>3+</sup>/Fe<sup>2+</sup> mapping at the thin section scale and comparison with XANES mapping: Application to a garnet-bearing metapelite from the Sambagawa metamorphic belt (Japan). *Journal of Metamorphic Geology*, *24*(7), 669–683.
- Vidal, O., Parra, T., & Vieillard, P. (2005). Thermodynamic properties of the Tschermak solid solution in Fe-chlorite: Application to natural examples and possible role of oxidation. *American Mineralogist*, *90*(2–3), 347–358.
- Viegas, G., Menegon, L., & Archanjo, C. (2016). Brittle grain-size reduction of feldspar, phase mixing and strain localization in granitoids at mid-crustal conditions (Pernambuco shear zone, NE Brazil). *Solid Earth*, *7*(2), 375–396.
- Walters, J. B., & Kohn, M. J. (2017). Protracted thrusting followed by late rapid cooling of the Greater Himalayan Sequence, Annapurna Himalaya, Central Nepal: Insights from titanite petrochronology. *Journal of Metamorphic Geology*, *35*(8), 897–917.
- Wassmann, S., & Stöckhert, B. (2013). Rheology of the plate interface—Dissolution precipitation creep in high pressure metamorphic rocks. *Tectonophysics*, *608*, 1–29.
- Wenning, Q. C., Berthet, T., Ask, M., Zappone, A., Rosberg, J., & Almqvist, B. S. G. (2017). Image log analysis of in situ stress orientation, breakout growth, and natural geologic structures to 2.5 km depth in central Scandinavian Caledonides: Results from the COSC-1 borehole. *Journal of Geophysical Research: Solid Earth*, *122*, 3999–4019. <https://doi.org/10.1002/2016JB013776>
- Wheeler, J., Prior, D., Jiang, Z., Spiess, R., & Trimby, P. (2001). The petrological significance of misorientations between grains. *Contributions to Mineralogy and Petrology*, *141*(1), 109–124.
- Wintsch, R. P., Christoffersen, R., & Kronenberg, A. K. (1995). Fluid-rock reaction weakening of fault zones. *Journal of Geophysical Research*, *100*(B7), 13,021–13,032.
- Wright, S. I., Nowell, M. M., & Field, D. P. (2011). A review of strain analysis using electron backscatter diffraction. *Microscopy and Microanalysis*, *17*(3), 316–329. <https://doi.org/10.1017/S1431927611000055>
- Zachrisson, E., & Sjöstrand, T. (1990). Bedrock Map 22E Frostviken. Sveriges Geologiska Undersökning (SGU) Ai 44, Scale 1: 50,000.
- Zwart, H. J. (1975). Structure and metamorphism in the Seve-Köli Nappe Complex (Scandinavian Caledonides) and its implications concerning the formation of metamorphic nappes. *Annales de La Société Géologique de Belgique*, 129–144.